Sedimentary protolith and high-P metamorphism of oxidized manganiferous quartzite from the Lanterman Range, northern Victoria Land, Antarctica

Taehwan Kim[1,2], **Yoonsup Kim**[3], **Simone Tumiati**[4], **Daeyeong Kim**[1], **Keewook Yi**[5], and **Mi Jung Lee**[1]

[1]Division of Earth Sciences, Korea Polar Research Institute, Incheon, 21990, Republic of Korea
[2]Department of Earth Science Education, Korea National University of Education,
Cheongju, 28173, Republic of Korea
[3]Department of Earth and Environmental Sciences, Chungbuk National University,
Cheongju, 28644, Republic of Korea
[4]Dipartimento di Scienze della Terra, Università degli Studi di Milano, via Mangiagalli 34, 20133, Milan, Italy
[5]Research Center for Geochronology and Isotope Analysis, Korea Basic Science Institute,
Cheongju, 28119, Republic of Korea

Correspondence: Taehwan Kim (taehwan.kim@knue.ac.kr)

Abstract. We investigated the mineral assemblage, mineral and bulk-rock chemistry, and zircon U–Pb age of a manganiferous quartzite layer in the Lanterman Range, northern Victoria Land, Antarctica. The mineral assemblage consists primarily of phengite and quartz, along with spessartine-rich garnet, Mn^{3+} and rare earth element–yttrium (REY)-zoned epidote-group minerals, and titanohematite. Mineral inclusions such as tephroite, rutile and pyrophanite are hosted in porphyroblasts of the latter three minerals and suggest prograde blueschist-facies to low-T eclogite-facies metamorphism (M_1). Epidote-group minerals commonly exhibit multiple growth zones of piemontite and/or epidote (M_1), REY-rich piemontite (M_2), REY-rich epidote (M_3), and epidote (M_4) from core to rim. Pseudobinary $f O_2$–X diagrams at constant P–T support the stability of an epidote-group mineral-bearing assemblage under highly oxidized conditions during prograde M_2 to peak M_3 metamorphism. In marked contrast, tephroite-bearing assemblages (M_1) are limited to relatively reduced environments and Mn-rich, silica-deficient bulk-rock compositions. Mn nodules have such characteristics, and the contribution of this hydrogenous component is inferred from bulk-rock chemical features such as a strong positive Ce anomaly. The major-element composition of the manganiferous quartzite suggests a protolith primarily consisting of a mixture of chert and pelagic clay. The presence of rare detrital zircons supports terrigenous input from a craton and constrains the maximum time of deposition to be ca. 546 Ma. The lack of arc-derived detrital zircons in the quartzite and the predominance of siliciclastic metasedimentary rocks among the surrounding rocks suggest that the deep-sea protolith was most likely deposited in an arc/back-arc setting at a continental margin. High-P metamorphism associated with terrane accretion during the Ross orogeny took place in the middle Cambrian (ca. 506 Ma), broadly coeval with the metamorphic peak recorded in the associated high-P rocks such as mafic eclogites. Finally, it is noteworthy that the high-P manganiferous quartzite was amenable to exhumation because the paleo-position of the protolith was likely distal from the leading edge of the downgoing slab.

1 Introduction

Oxidized, deep-sea siliceous sediments rich in manganese are commonly found as a precursor of spessartine-rich quartzitic rocks (e.g., Mottana, 1986; Abs-Wurmbach and Peters, 1999). Occurrences of Mn-rich quartzose rock have been reported particularly in high- to ultrahigh-P terranes, such as the Hellenides blueschist belt on the island of Andros, Greece (Reinecke et al., 1985; Reinecke, 1986), and the meta-ophiolite belt in the Zermatt–Saas zone of the Western Alps (Reinecke, 1998; Rubatto et al., 1998; Tumiati et al., 2010). However, fundamental questions still remain largely unsolved concerning the petrologic and tectonic nature of the sedimentary protoliths and metamorphism. This is because of (1) rare occurrence, (2) diverse source reservoirs, (3) variable oxidation states and (4) metamorphic overprinting (e.g., Reinecke et al., 1985; Tumiati et al., 2010). Further complexity arises from the different names used to describe the spessartine–quartz-rich metasedimentary rocks, "coticules" in Belgium (Herbosch et al., 2016) and "gondites" in India (Melcher, 1995). Coticules are fine-grained, mica-rich yellowish rocks which have likely been used for whetstones since the time of the Roman Empire. Gondites, on the other hand, are meta-arenaceous and meta-argillaceous rocks commonly associated with ores. In order to avoid any confusion, we use the term Mn-rich quartzose metasedimentary rock or manganiferous quartzite rather than these historical or descriptive ones.

Manganese is known to be mobile during water–rock interactions, with high solubility in hydrothermal fluids (Edmond et al., 1982). The primary source of silica in the Mn-rich quartzose (meta)sedimentary rocks is generally considered to be biogenic, particularly radiolarian chert (Mottana, 1986). Variable contributions of detrital siliciclastics also played a role in the formation of these peculiar sedimentary rocks (Coombs et al., 1985; Reinecke et al., 1985; Mottana, 1986). Hydrogenous precipitation is another significant process, where Mn-rich sedimentary rocks could serve as key beds in stratigraphic correlation (e.g., Thomson, 2001; Herbosch et al., 2016). The combination of these variable source components in various proportions contributed to the formation of the Mn-rich siliceous sedimentary rocks.

The Mn-rich quartzites or metasedimentary rocks contain mineral assemblages of braunite ($Mn^{2+}Mn_6^{3+}SiO_{12}$), rhodochrosite ($Mn^{2+}CO_3$), sursassite ($Mn^{2+}Al_3Si_3O_{11}(OH)_3$), tephroite ($Mn_2^{2+}SiO_4$), hausmannite ($Mn^{2+}Mn_2^{3+}O_4$), rhodonite/pyroxmangite ($Mn^{2+}SiO_3$), "alurgite" (Mn-bearing phengite), "violan" (Mn-bearing omphacite), piemontite ($Ca_2Al_2Mn^{3+}Si_3O_{12}(OH)$) and spessartine ($Mn_3^{2+}Al_2Si_3O_{12}$) (see Tumiati, 2005, and references therein). In particular, piemontite-bearing quartzites with a talc–phengite assemblage have been studied extensively as an indicator of high-P metamorphism (e.g., Massonne and Schreyer, 1989). The ultrahigh-P mineral

coesite has even been discovered in layers of manganiferous quartzite at Lago di Cignana in the Zermatt–Saas zone (Reinecke, 1998). The varying oxidation states of Mn are petrologically significant with regard to redox conditions during metamorphism (Abs-Wurmbach and Peters, 1999; Tumiati et al., 2015). The preservation of Mn-silicate assemblages necessitates uncommon high-fO_2 conditions throughout the metamorphic cycle (Abs-Wurmbach and Peters, 1999; Tumiati et al., 2015).

In this study, we analyzed the bulk-rock and mineral chemistry, conducted pseudosection modeling, and determined the U–Pb geochronology of manganiferous quartzite. This quartzite occurs as centimeter- to decimeter-thick layers hosted within mafic eclogites and phengite-bearing quartzofeldspathic schists/gneisses from the Lanterman Range in northern Victoria Land (NVL), Antarctica. The aims of this study are (1) to unravel the origin and depositional setting of the protolith; (2) to demonstrate high-P paragenesis of the epidote-group mineral, phengite and garnet; (3) to constrain the oxidation state of the Mn^{3+}–Fe^{3+}-bearing mineral assemblages; (4) to estimate the depositional and metamorphic ages from the U–Pb dating of zircon; and (5) to finally discuss tectonic implications of the petrogenesis.

2 Geological background

At the final stage of the Gondwana assembly, subduction of the Paleo-Pacific and Iapetus plates along the periphery of Gondwana resulted in the formation of the Andean-type Terra Australis orogen (Fig. 1a) (Boger and Miller, 2004; Cawood, 2005; Foden et al., 2006). This accretionary tectonics was represented by the Ross orogeny in East Antarctica, giving rise to a prolonged continental arc system spanning the late Neoproterozoic to Early Ordovician times (e.g., Kleinschmidt and Tessensohn, 1987; Rocchi et al., 2011; Goodge, 2020). The exposed crustal root of the Ross orogen forms the Transantarctic Mountains, which currently serve as a physiographic boundary between East and West Antarctica (e.g., Stump, 1995; Faure and Mensing, 2010).

Northern Victoria Land, situated at the Pacific end of the Ross orogen, is primarily composed of three NW-trending, fault-bounded blocks: the Wilson, Bowers and Robertson Bay terranes from onshore to offshore (Fig. 1b) (e.g., Weaver et al., 1984; Bradshaw et al., 1985; GANOVEX Team, 1987). The inboard Wilson terrane formed a continental arc complex near the eastern edge of the Polar Plateau. The terrane mainly consists of low-P/T metasedimentary rocks subjected to conditions ranging from low-grade to migmatitic stages, along with syn- to post-orogenic plutons of mostly middle Cambrian to Early Ordovician age (Granite Harbour intrusives) (e.g., Borg et al., 1987; Palmeri, 1997; Rocchi et al., 2004; Talarico et al., 2004; Bomparola et al., 2007; Giacomini et al., 2007). The Bowers terrane is a broadly NW-trending elongate belt of $\sim$ 20–50 km width. It primar-
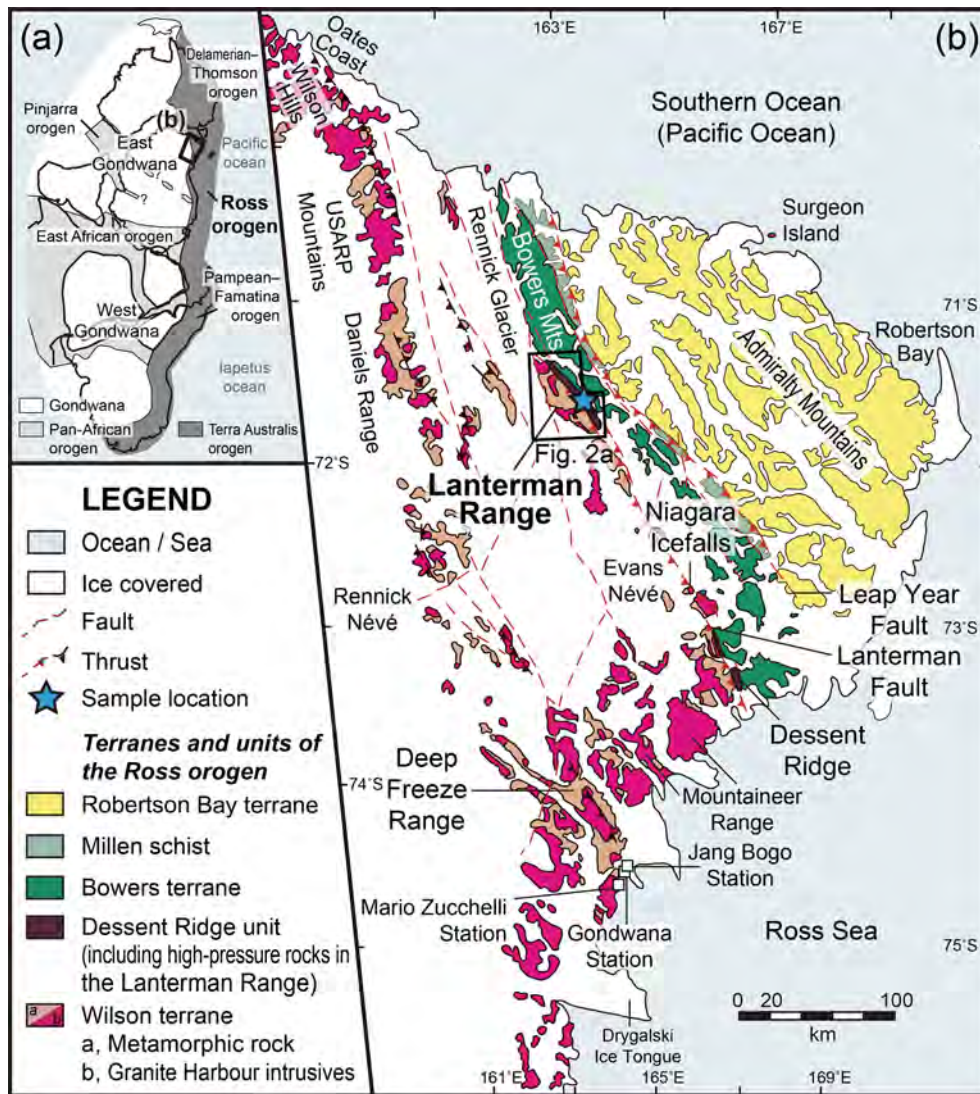
Figure 1. (a) Schematic map exhibiting the distribution of the Terra Australis orogen along the Gondwana margin. The Antarctic segment of the orogen is the Ross orogen of the Transantarctic Mountains. A box denotes the location of northern Victoria Land (NVL) enlarged in **(b)**. **(b)** Tectonic province map of NVL modified from Läufer et al. (2011), showing key lithotectonic elements including three terranes and two intervening metamorphic belts. The region in the black box is enlarged in Fig. 2a. The post-Ross rocks were omitted for clarity.

ily comprises weakly metamorphosed rocks, in stratigraphic order; early to middle Cambrian volcanic–volcaniclastic sequences of island arc or back-/fore-arc settings; and late Cambrian to Early Ordovician molasse-type siliciclastic sediments (e.g., Weaver et al., 1984; Wodzicki and Robert, 1986; Jago et al., 2019). The outboard Robertson Bay terrane consists of variably folded, flysch-type monotonous turbiditic sequences with > 3000 m thickness of late Cambrian to Early Ordovician age (e.g., Field and Findlay, 1983; Dallmeyer and Wright, 1992; Zhen et al., 2019).

The low-P/T gneisses predominate to the west of the Wilson terrane and transform into medium- to high-P/T schists and gneisses to the east in the mountainous regions. It is inferred that the Rennick Glacier overlies a profound disconti-

nuity of metamorphic grade in the Wilson terrane (Figs. 1b, 2a) (Grew et al., 1984; Kleinschmidt and Tessensohn, 1987). Such an increase in the P/T ratio is particularly noticeable in the Lanterman, Salamander and Mountaineer ranges. The Lanterman Range is located in the central part of the Wilson–Bowers terrane boundary, which is defined by the Lanterman Fault (Figs. 1b, 2a). The Dessent Ridge unit to the west of the Lanterman Fault comprises medium- to high-P/T rocks and is mainly composed of medium-P amphibolites and metapelites in the southeast (e.g., Scambelluri et al., 2003; Palmeri et al., 2012) and eclogite-facies rocks of the Lanterman Range in the northwest (e.g., Di Vincenzo et al., 1997; Palmeri et al., 2003) (Fig. 2a). Three metamorphic units are distinguished from west to east in the Lanterman
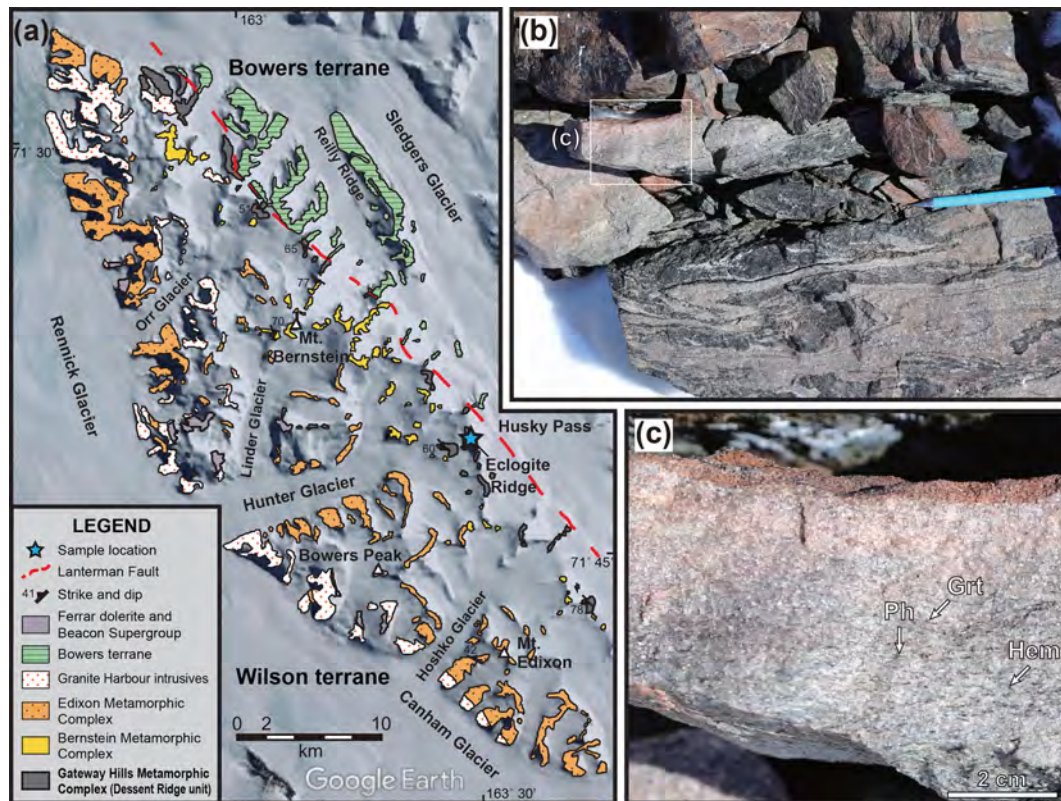
Figure 2. (a) Geological map of the Lanterman Range, northern Victoria Land, modified from GANOVEX Team (1987) and Talarico et al. (1998), put on a © Google Earth image. A blue star denotes the Eclogite Ridge where a manganiferous quartzite sample was collected (70°40.56′ S, 163°27.726′ E). **(b, c)** Outcrop photographs showing field occurrence of the quartzite and associated mafic–felsic layers. A pinkish quartzite horizon intercalated with (garnet) amphibolite and quartzofeldspathic schist layers is in **(b)**. Complex fold structures and alternations of the mafic and felsic rocks are consistent with pervasive ductile deformation. A box is enlarged in **(c)**. Medium-grained quartzite showing pinkish garnet, brownish phengite and dark titanohematite (Hem) embedded in the quartz-dominant matrix is in **(c)**. Mineral abbreviations are after Whitney and Evans (2010).

Range: the low-P Edixon, medium-P Bernstein and high-P Gateway Hills Metamorphic complexes (Talarico et al., 1998, 2004). The latter unit contains tectonic lenses of eclogite, amphibolite and meta-ultramafic rock (e.g., Ricci et al., 1996; Di Vincenzo et al., 1997).

High-P metamorphic rocks including the manganiferous quartzites occur along a small ridge of the Lanterman Range known as the Eclogite Ridge (Fig. 2a) (Ricci et al., 1996; Capponi et al., 1997). Eclogites, amphibolites and meta-ultramafic rocks in the Lanterman Range commonly occur as lenses or discontinuous layers, with a thickness of up to tens of meters, enclosed by country rocks of mostly garnet–phengite quartzofeldspathic gneisses (Ricci et al., 1996; Capponi et al., 1997). Two different P–T paths have been proposed by Di Vincenzo et al. (2016) for high- and medium-T eclogites (e.g., Carswell, 1990). One pertains to the hotter eclogites ($\sim$800 °C) featuring coesite-stable peak pressure with an unknown prograde path (Di Vincenzo et al., 1997; Ghiribelli et al., 2002), while the other relates to the colder eclogites ($\sim$700 °C) with amphibolite-facies prograde

stages followed by an eclogite-facies peak (Di Vincenzo et al., 2016; Kim et al., 2019). The timing of the eclogite-facies metamorphism was dated in the range of ca. 530–500 Ma, culminating at ca. 500 Ma (Di Vincenzo et al., 1997, 2016; Kim et al., 2019) (Fig. 3). The crystallization ages of rift-related gabbroic protoliths were estimated from the igneous cores of zircon in the colder eclogites at ca. 600–590 Ma (Kim et al., 2023). Retrograde cooling and exhumation rates under the amphibolite-facies conditions were estimated to be > 30 °C Myr^{-1} and 2–5 km Myr^{-1}, respectively (e.g., Di Vincenzo and Palmeri, 2001).

Palmeri et al. (2003) proposed that the host garnet–phengite quartzofeldspathic schists and gneisses underwent the prograde amphibolite- and peak eclogite-facies metamorphism at $\sim$5–8 kbar and 500 °C and in the coesite-stable conditions, respectively. The authors suggested phengite breakdown into biotite–plagioclase symplectite during the amphibolite-facies retrogression. Comparable phengite decomposition textures were observed in the megacrystic phengite-bearing quartz veins that crosscut the retrogressed
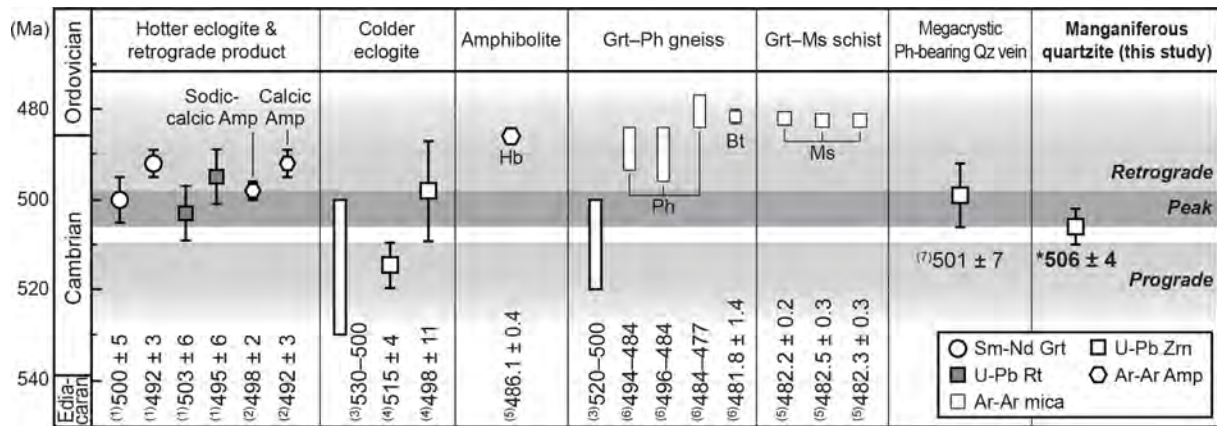
Figure 3. Timeline diagram representing metamorphic stages of the high-P rocks in the Gateway Hills Metamorphic Complex of the Lanterman Range modified after Kim and Lee (2023). Geochronological data are from this study (∗) and those available from the literature (weighted mean ages in Ma at 2σ confidence level, except for 5): (1) Di Vincenzo et al. (1997), (2) Di Vincenzo and Palmeri (2001), (3) Di Vincenzo et al. (2016), (4) Kim et al. (2019), (5) Goodge and Dallmeyer (1996), (6) Di Vincenzo et al. (2001), and (7) Kim and Lee (2023). Boxes for (3) and (6) denote ranges of spot dates. Error bars of (5) are not shown because of their size being smaller than that of symbol. Time intervals are marked for the eclogite-facies prograde-peak and amphibolite-facies retrograde stages. Mineral abbreviations are after Whitney and Evans (2010).

eclogites and record high-P zircon growth at ca. 500 Ma (Kim and Lee, 2023) (Fig. 3). The celadonite-rich phengite in the (ultra)high-P schists and gneisses yielded ^{40}Ar/^{39}Ar ages slightly younger than 500 Ma, whereas the relatively celadonite-poor neoblasts which are aligned parallel to or discordantly to the foliation gave ca. 482–478 Ma in dating the greenschist-facies retrogression (Di Vincenzo et al., 2001) (Fig. 3). Di Vincenzo et al. (2016) extended a time frame of the eclogite-facies metamorphism of the quartzofeldspathic schists and gneisses on the basis of scattered zircon spot dates ranging from ca. 520 Ma to ca. 500 Ma (Fig. 3). The tectonic setting of the protoliths of the (ultra)high-P quartzofeldspathic schists and gneisses has been suggested to be arc/back arc; this proposition is based upon largely siliciclastic compositions, their interlayering with meta-mafic rocks of possibly basalt flow/dike origin and the varying geochemical affinities of the meta-mafic rocks ranging from E-MORB (enriched mid-ocean ridge basalt) or T-MORB (transitional mid-ocean ridge basalt) to calc-alkaline signatures (Palmeri et al., 2003; Rocchi et al., 2011). Capponi et al. (1997) mapped the occurrence of garnet-bearing pinkish manganiferous quartzites as thin layers ranging from centimeters to decimeters in thickness, aligned parallel to the regional foliation trending NW to NNW. Garnet is idioblastic and rich in spessartine, and quartz is granoblastic showing weak alignment parallel to the regional foliation. Capponi et al. (1997) speculated that the relationships of intercalation with meta-mafic and meta-ultramafic rocks suggest an ophiolite affinity of the manganiferous quartzites.

3 Sample description and petrography

Manganiferous quartzite sample 23-1F was collected from the northern part of "outcrop 4" according to the geological map of the Lanterman Range produced by Capponi et al. (1997). The sample location matches that of Di Vincenzo et al. (2016) and Kim et al. (2019) where medium-grained colder eclogites were reported. It is situated several hundred meters northward of the locality of fine-grained hotter eclogite (Di Vincenzo et al., 1997) (Fig. 2a). The Mn-rich quartzose metasedimentary rocks are volumetrically minor relative to the meta-mafic blocks and the surrounding garnet–phengite quartzofeldspathic and hornblende–biotite gneisses/schists in the study area and are characterized by a pinkish tinge visible to the naked eye (Fig. 2b, c). The centimeter-to decimeter-thick concordant layers of the manganiferous quartzite are interleaved within the garnet–phengite quartzofeldspathic and amphibolitic schists (Fig. 2b, c; see also Capponi et al., 1997). These schists of contrasting lithologies commonly show intensive high-T deformation features such as isoclinal folding and mafic boudin formation, whereas the pinkish medium-grained manganiferous quartzites are moderately foliated (Fig. 2b, c). The major foliation of the quartzite layer is well-defined by flaky phengite and elongate-shaped titanohematite.

Mineral assemblages of the manganiferous quartzite sample are represented by a Mn-bearing epidote-group mineral (0.5 %) (nomenclature after Armbruster et al., 2006) + spessartine-rich garnet (1.5 %) + titanohematite (1 %) + phengite (12 %) + quartz (85 %), together with subordinate amounts of rutile, chlorite, plagioclase, K-feldspar, zircon, monazite and apatite (Fig. 4a). Three types

of garnet are discernible on the basis of grain size and morphology. The first type of garnet (Grt I) is hypidioblastic and has an average size of $\sim 500\,\mu m$ (Figs. 4b, 5a). Grt I contains small numbers of inclusions such as rutile and quartz. Skeletal garnet, Grt II, is coarser-grained than Grt I and is commonly associated with chlorite at the margin (Figs. 4c, 5b). Fine-grained hypidio- to xenoblastic garnet, Grt III, mostly $< 200\,\mu m$, is inclusion-poor and commonly elongate in shape with its longest dimension subparallel to the foliation (Fig. 4d).

Epidote-group minerals occur as three types: (1) blade-shaped porphyroblasts, (2) xenoblasts enclosing Grt III and (3) euhedral allanite neoblasts. The first type exhibits a prominent compositional zonation with an inclusion-rich core, inclusion-poor mantle and outermost rim (Figs. 4b, 6). The core encloses inclusions of phengite, rutile, chlorite, titanohematite, quartz and Mn silicate phases such as tephroite (Fig. 6). Allanite neoblasts commonly exhibit fractures and contain mineral inclusions such as phengite, chlorite, titanohematite and quartz. Rutile occurs as an inclusion within Grt I and titanohematite, whereas ilmenite and pyrophanite ($Mn^{2+}TiO_3$) within titanohematite occur as exsolution lamellae (Fig. 5a). The grain size of phengite flakes varies largely, ranging from several hundred micrometers to 10 mm in their longest dimension. Marginal breakdown textures are negligible in phengite, in marked contrast to those observed in the surrounding garnet–phengite gneisses (Palmeri et al., 2003) and megacrystic phengite-bearing quartz veins (Kim and Lee, 2023). Secondary K-feldspar and albite form discrete bands (Fig. 4a, b, c). Quartz is commonly granoblastic and moderately aligned parallel to the major foliation (Fig. 4). Weak deformation bands and undulose extinction are apparent in quartz.

4   Analytical methods

Concentrations of the major and trace elements in manganiferous quartzite sample 23-1F were determined using inductively coupled plasma optical emission system and mass spectrometer methods, respectively, employing lithium metaborate–tetraborate fusion at Activation Laboratories Ltd., Ontario, Canada. Mineral compositions were analyzed using a JEOL JXA-8530F field-emission (FE) electron microprobe housed at the Korea Polar Research Institute (KOPRI), with 15 kV accelerating voltage, 10 nA beam current, 3–5 μm beam diameter and 20 s counting times. The compositions of epidote-group minerals particularly rich in rare earth element and yttrium (REY) were measured following the analytical conditions of Kim et al. (2009). Standard materials used for the calibration include natural silicates and synthetic phosphates and oxides. Matrix correction was performed using the ZAF method. The X-ray mapping was conducted with an accelerating voltage of 15 kV, beam current of 200 nA, dwell time per pixel of 150 ms, step size

of 3 μm and focused beam. Representative analyses of garnet, epidote-group mineral, phengite, chlorite, feldspars and oxides are given in Table S1.

A thin section of sample 23-1F cut parallel to lineation and perpendicular to foliation was coated with 10–15 nm thick carbon after mechanical and chemical polishing. The lattice preferred orientations (LPOs) of quartz were measured using electron backscatter diffraction (Oxford Symmetry S2) attached to a JEOL JSM-7200F-LV FE scanning electron microscope (SEM) housed at KOPRI. Analytical settings include an accelerating voltage of 20 kV, working distance of 23 mm and beam current of 10 nA. Automated montage mapping (10 μm step size) was performed on the whole area of the section (ca. $3.5 \times 2.5\,cm$), and the raw data were processed to compile montaged maps using the AZtec software. Noise reduction was conducted by filling the non-indexed pixels from five to eight identical neighbors using the AZtecCrystal software. Pole figures of one point per grain data were plotted on lower-hemisphere equal-area projections employing an orientation distribution function with half width of 15°.

Zircon separates were collected from sample 23-1F, using the conventional heavy-liquid technique of Cheong et al. (2013), and were mounted in 25.4 mm epoxy disks together with standard materials: zircon SL13 and FC-1 for measuring the U concentration ($\mu g\,g^{-1}$; Claoué-Long et al., 1995) and for calibrating $^{206}Pb/^{238}U$ ratios ($^{206}Pb^*/^{238}U = 0.1859$; Paces and Miller, 1993), respectively. Cathodoluminescence (CL) images of individual crystals were obtained using a JEOL JSM-6610LV SEM housed at the Korea Basic Science Institute (KBSI). The U–Th–Pb isotopic compositions of zircon were measured using the KBSI sensitive high-resolution ion microprobe, SHRIMP-IIe. The analytical protocol for zircon followed that of Williams (1998). All isotopes were measured using a primary O_2^- beam with $\sim$ 3–5 nA and a $\sim$ 25 μm diameter spot. Common Pb contributions to total Pb counts were corrected using the ^{204}Pb and ^{207}Pb correction methods for ages older and younger than 1.0 Ga, respectively, with a model Pb composition (Cumming and Richards, 1975; Williams, 1998). The software programs SQUID2 (Ludwig, 2009) and Isoplot/Ex (Ludwig, 2008) were used for the age calculation and data processing, respectively. Individual spot analyses and weighted mean $^{206}Pb/^{238}U$ ages of zircon are quoted at 1σ and 2σ confidence levels, respectively.

5   Mineral chemistry and quartz LPO

5.1   Garnet

Mineral formulae of garnet are calculated on the basis of five non-tetrahedral cations following the procedure of Cenki-Tok and Chopin (2006) in order to account for valence states of Fe and Mn and a possible hydrogarnet component. Garnet
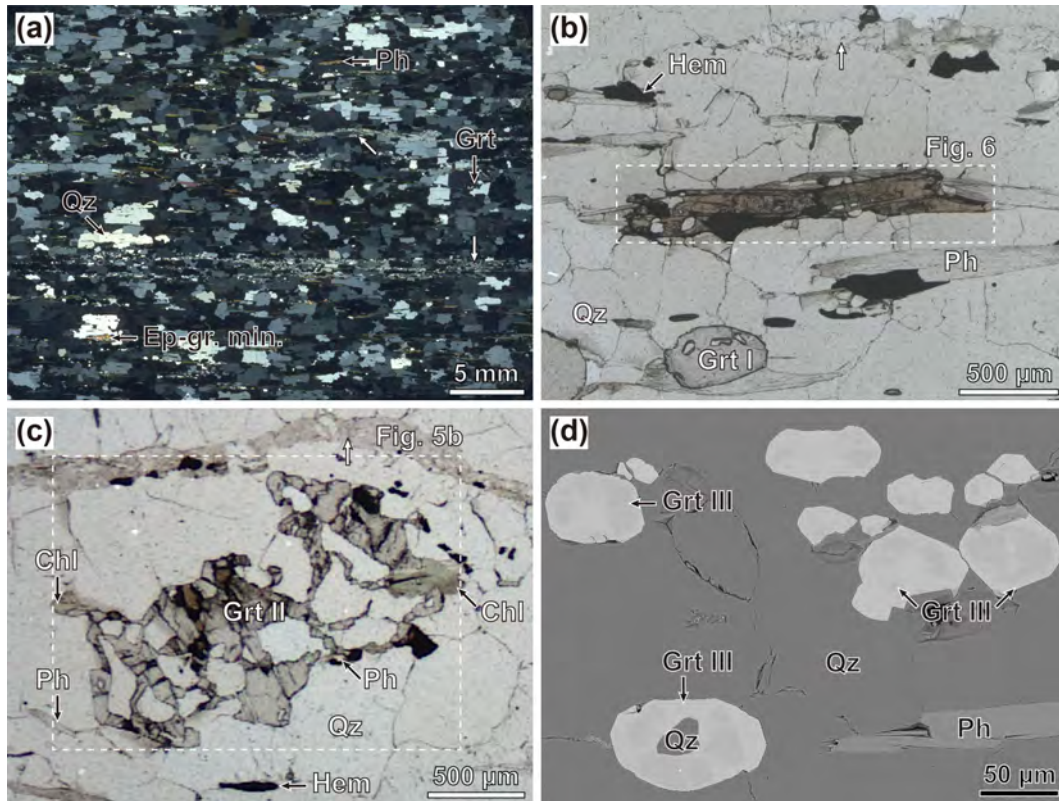
Figure 4. Photomicrographs **(a–c)** and backscattered electron image **(d)** of manganiferous quartzite sample 23-1F showing mineral parageneses and occurrences of porphyroblasts. Photomicrographs were taken under cross-polarized light **(a)** and plane-polarized light **(b, c)**. White arrows denote albite–K-feldspar-rich layers. **(a)** Representative mineral assemblage mainly consisting of garnet, epidote-group mineral (Ep-gr. min.), phengite, titanohematite (Hem) and quartz. **(b)** Subhedral epidote-group mineral porphyroblast zoned in Mn^{3+}. The X-ray chemical maps of the grain are shown in Fig. 6. Porphyroblasts of subhedral Grt I, flaky phengite and titanohematite are also shown. **(c)** Xenoblastic Grt II partly rimmed by chlorite. The X-ray chemical maps of the grain are shown in Fig. 5b. **(d)** Subhedral, fine-grained Grt III. The grains are elongate in shape and oriented subparallel to the major foliation (horizontal). Mineral abbreviations are after Whitney and Evans (2010).

porphyroblasts in the manganiferous quartzite sample are rich in spessartine with relatively constant grossular contents ($Grs = Ca / (Fe^{2+} + Mg + Ca + Mn) = 0.09–0.15$). Grt I preserves an inner domain or core of relatively homogeneous composition ($Sps = Mn / (Fe^{2+} + Mg + Ca + Mn) = 0.59–0.65$; $Alm = Fe^{2+} / (Fe^{2+} + Mg + Ca + Mn) = 0.00–0.02$; $X_{Fe} = Fe^{2+} / (Fe^{2+} + Mg) = 0.00–0.07$) (Figs. 5a, 7a). An abrupt increase in X_{Fe} accompanied by a slight decrease in Mn ($Sps = 0.57–0.58$; $Alm = 0.14–0.18$; $X_{Fe} = 0.49–0.50$) is conspicuous at the narrow outermost rim ($< 50\,\mu m$ width). Compositional variations in xenoblastic Grt II are similar to those of Grt I, exhibiting a low-X_{Fe} inner domain ($Sps = 0.63–0.65$; $Alm = 0.01–0.03$; $X_{Fe} = 0.04–0.11$) enveloped by a higher-X_{Fe} outer domain ($Sps = 0.56–0.58$; $Alm = 0.07–0.13$; $X_{Fe} = 0.58–0.78$) (Figs. 5b, 7a). Fine-grained Grt III exhibits much higher Fe^{2+} contents compared to those of Grt I and Grt II; its inner domain ($Sps = 0.54–0.58$; $Alm = 0.08–0.26$; $X_{Fe} = 0.26–0.46$) is less Fe-rich than its outer domain ($Sps = 0.49–0.57$; $Alm = 0.15–0.31$; $X_{Fe} = 0.50–0.79$) (Fig. 7a). All types of

garnet are commonly typified by the brighter outermost part or rim in backscattered electron images. The average Si content of the analyzed garnet is 2.99 atoms per formula unit (apfu), suggesting a negligible hydrogarnet component. The andradite component is low (Adr < 0.04).

5.2 Epidote-group minerals

Epidote-group minerals commonly exhibit systematic zoning patterns, with compositions spanning piemontite to epidote (Armbruster et al., 2006). Ce and Mg zoning patterns in X-ray maps are similar to each other but antithetic to that of Ca (Fig. 6). The inner domains are divided into two compositional groups: piemontite ($Pmt = Mn^{3+} / (Fe^{3+} + Mn^{3+} + Al^{VI} - 2) = 0.46–0.59$; $Ep = Fe^{3+} / (Fe^{3+} + Mn^{3+} + Al^{VI} - 2) = 0.37–0.43$) and epidote ($Pmt = 0.19–0.48$; $Ep = 0.50–0.66$) (Figs. 6, 7b). These inner domains are low in REY abundances ($\Sigma REY = La + Ce + Pr + Nd + Gm + Gd + Y = 0.02–0.10$ apfu) (Fig. 8) and relatively high in SrO and PbO contents ($0.57\,wt\% – 0.92\,wt\%$ and $0.17\,wt\% – 0.32\,wt\%$, respectively). The outer domains with
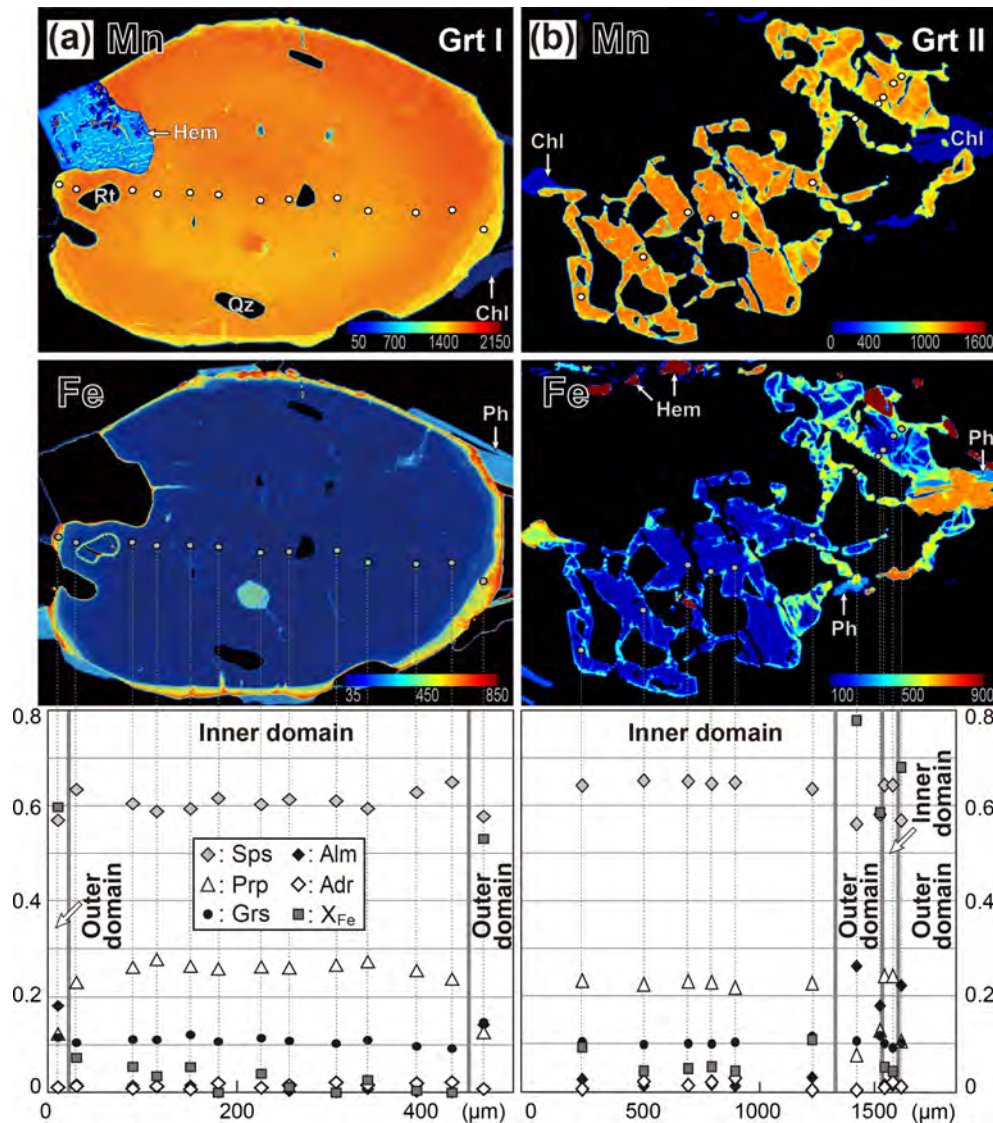
Figure 5. X-ray maps and compositional profiles of garnet porphyroblasts (**a** Grt I and **b** Grt II). The Ti X-ray map for titanohematite and its inclusions is shown with bluish colors at the top left in the Mn X-ray map in **(a)**. Minerals with X-ray counts that are too high and low are shown in black for clarity; for example, titanohematite (Hem) and other Fe-rich oxides in the Fe map of **(a)**. Rutile inclusion shows a similar intensity to that of host Mn-rich garnet in the Fe map because garnet is extremely low in FeO ($< 1\%$; Table S1 in the Supplement). In **(a)**, two small lower-Mn inclusions and one higher-Fe inclusion near the garnet center are impurities. Mineral abbreviations are after Whitney and Evans (2010).

higher REY contents consist of two zones: (1) outer zone 1 of REY-rich piemontite (Pmt = 0.58–0.62; Ep = 0.38–0.42) and (2) outer zone 2 of REY-rich epidote composition (Pmt = 0.23–0.42; Ep = 0.55–0.71) (Figs. 6, 7b, 8). An abrupt increase in REY and Th and a slight decrease in PbO are conspicuous in the former (ΣREY = 0.19–0.25 apfu; ThO$_2$ = 0.14 wt %–0.32 wt %; PbO = 0.11 wt %–0.24 wt %). Outer zone 2 contains higher REY and Th (ΣREY = 0.32–0.39 apfu; ThO$_2$ = 0.31 wt %–0.66 wt %), PbO (0.09 wt %–0.53 wt %), and Na$_2$O contents (0.11 wt %–0.41 wt %). SrO contents are comparable for outer zones 1 (0.27 wt %–

0.40 wt %) and 2 (0.21 wt %–0.40 wt %). The outermost domains are near-epidote end-member in their composition (Pmt = 0.09–0.10; Ep = 0.75–0.84) and lowest in REY contents (ΣREY = 0.06–0.08 apfu) among the compositional domains of the epidote-group mineral (Fig. 8). The chondrite-normalized REY patterns of the epidote-group mineral are characterized by a positive Ce anomaly (Fig. 8).

5.3 Phengite

The celadonite contents of phengite vary abruptly from the inner (Si = 3.23–3.34 apfu) to outer (Si = 3.14–3.27 apfu)
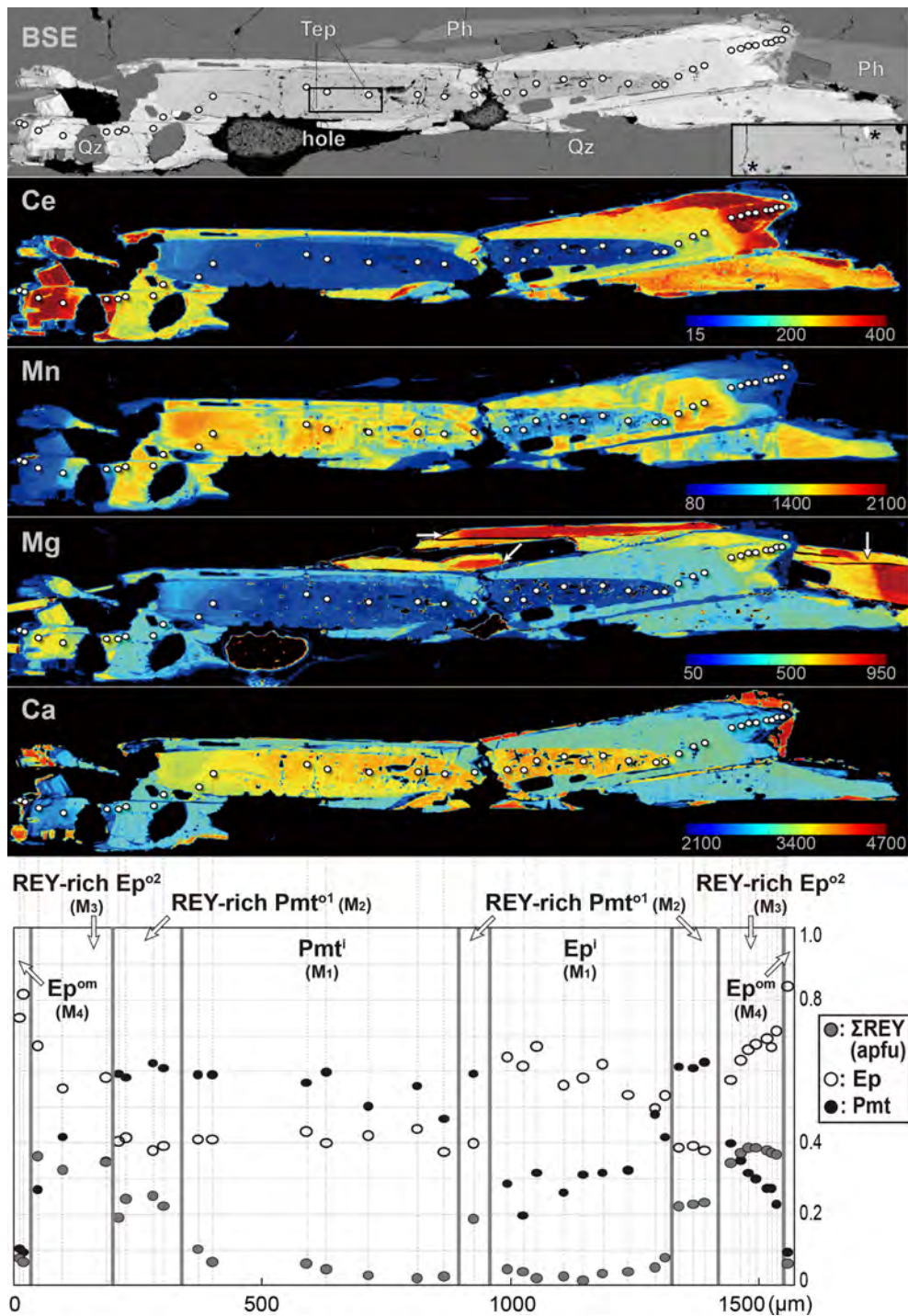
Figure 6. Backscattered electron (BSE) image, X-ray maps and compositional profile of a subhedral porphyroblast of epidote-group mineral. Four distinct compositional domains are defined on the basis of Mn^{3+}, Fe^{3+}, and rare earth element and yttrium (REY) contents: inner domain (i; piemontite and epidote), outer zone 1 (o1; REY-rich piemontite), outer zone 2 (o2; REY-rich epidote) and outermost domain (om; epidote). A box in the BSE image shows tephroite inclusions enlarged in the lower-right part of the image (asterisks). White arrows in the Mg map denote the celadonite zonation of phengite. Mineral abbreviations and epidote-group mineral nomenclatures are after Whitney and Evans (2010) and Armbruster et al. (2006), respectively; apfu, atoms per formula unit.
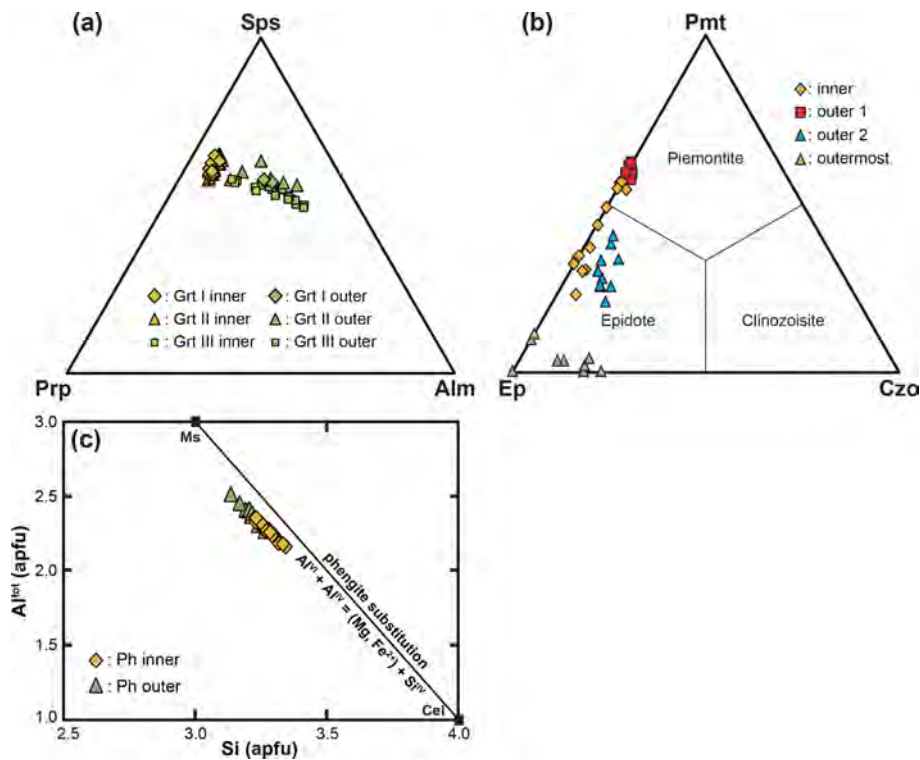
Figure 7. Compositional diagrams of **(a)** garnet, **(b)** epidote-group mineral and **(c)** phengite. Mineral abbreviations are after Whitney and Evans (2010); apfu, atoms per formula unit.
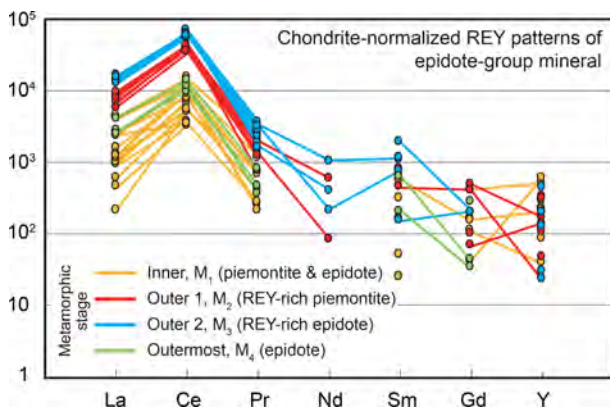

Figure 8. Chondrite-normalized (Sun and McDonough, 1989) rare earth element and Y (REY) patterns of epidote-group mineral.

domains (Figs. 6, 7c). Stoichiometric Fe^{3+} was not calculated because of possible octahedral vacancy and O–OH substitution (Page et al., 2007), although the excess Fe + Mg relative to Si ($= Fe + Mg - (Si - 3) = 0.10$–$0.13$ apfu) or the analytical points plotted below the Ms–Cel line in Fig. 7c indicate the presence of the ferri-muscovite component (e.g., Guidotti, 1984). Ti contents are slightly higher in the inner domains (0.05–0.09 apfu) than those in the outer do-

mains (0.03–0.06 apfu). The MnO content of phengite is low (0.01 wt %–0.27 wt %).

5.4   Tephroite

Two tephroite inclusions enclosed by the piemontite core of an epidote-group mineral porphyroblast were analyzed (Fig. 6). One inclusion of $\sim 7\,\mu m$ size yielded a reasonable result with near-end-member composition ($Tep = Mn / (Fe^{2+} + Mg + Ca + Mn) = 0.94$).

5.5   Chlorite

Chlorite is clinochlore in composition with 1.68 wt %–2.37 wt % MnO. The X_{Fe} of chlorite is in the range of 0.20–0.28.

5.6   Feldspar

The compositions of phengite-replacing feldspars are near-end-member albite ($An = Ca / (Ca + Na + K) = 0.02$–$0.05$) and K-feldspar ($Or = K / (Ca + Na + K) = 0.98$–$0.99$). No significant zonation is observed for plagioclase.

5.7   Oxides

Elongate titanohematite enclosing ilmenite and pyrophanite is Ti-rich in composition ($Hem = 0.86$–0.89;
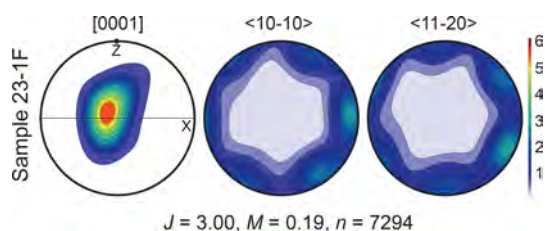
Figure 9. Lattice preferred orientations of quartz in quartzite sample 23-1F. The east–west direction corresponds to lineation (X), and the north–south direction is normal to foliation (Z). J, J index; M, M index; n, number of grains.

Ilm $= 0.11$–0.13). Ilmenite is rich in hematite component (Hem $= 0.14$; Ilm $= 0.85$). Pyrophanite consists of two compositional groups, Mn-rich ones (Hem $= 0.07$; Ilm $= 0.04$–0.06; Pph $= 0.88$–0.89) and Mn-poor ones (Hem $= 0.26$; Ilm $= 0.12$; Pph $= 0.62$).

5.8 Quartz fabric

Quartz LPOs of the analyzed quartzite sample exhibit a single cluster of [0001] around the y axis, and great circles of a axes ([10–10]) and poles to m planes ([11–20]) (Fig. 9). The LPO strength was quantified as the J and M index; the former is calculated as the second moment of the orientation distribution function (Bunge, 1982) and the latter as the difference between the distributions of uncorrelated misorientation angles for sample data and a random fabric (Skemer et al., 2005). The J index ranges theoretically from 1 to infinity for random and single-crystal LPO, respectively, and the M index from 0 to 1. The calculated J and M indices of quartz are 3.00 and 0.19, respectively.

6 Pseudosection modeling

In order to complement previous experimental studies on the Mn–Si–O ($\pm$ Al) system (Anastasiou and Langer, 1977; Keskinen and Liou, 1979; Abs-Wurmbach and Peters, 1999), we conducted thermodynamic modeling of the Mn–Ca–Fe–Al–Si–O system (Fig. 10). We calculated pseudosections in the Mn–Ca–Fe–Al–Si–O model system, using the Perple_X program (Connolly, 2005). The thermodynamic database of Holland and Powell (1998), updated in 2004 (hp04ver.dat), has been further modified by Tumiati et al. (2015) to include manganese oxides and end-member piemontite. Ideal mixing was assumed for epidote–piemontite solid solution. The garnet solution model is from Holland and Powell (1998). Pure end-member phases include braunite, tephroite, pyroxmangite, hematite, magnetite, quartz, kyanite, margarite, hedenbergite and H_2O.

Two fO_2–X pseudobinary diagrams were calculated at 8 kbar and 500 °C and 18 kbar and 550 °C for upper greenschist-facies (Fig. 10a) and prograde eclogite-facies

conditions, respectively (Fig. 10b), the latter being obtained from the colder eclogites in the study area (Kim et al., 2019). The model bulk-rock composition (X) ranges from pure SiO_2 ($X = 0$) to a compound ($X = 1$) consisting of 1 mol of garnet ($Sps_{81}Grs_{19}$) + 1 mol of epidote-group mineral ($Pmt_{50}Ep_{50}$) + 0.2 mol of tephroite which was estimated on the basis of inclusion relationships and mineral chemistries (Table S1). The amount of tephroite is apparently exaggerated in comparison to that observed in the thin section as micro-inclusions (Fig. 6) in order to increase bulk-rock MnO content and to highlight the phase relationships of Mn-bearing minerals (Tumiati et al., 2015).

Both modeling results under two different P–T conditions yielded a similar topology (Fig. 10). The spessartine–grossular–almandine garnet solid solution is stable over a wide range of both fO_2 and X values, except for extremely high fO_2 fields under the greenschist-facies condition (Fig. 10a). The stability of piemontite–epidote solid solution is limited to relatively oxidized fields. The tephroite-bearing, silica-undersaturated assemblages are stable at high-Mn bulk-rock compositions ($X > 0.8$) and in more reduced environments below the hematite–magnetite redox buffer (the fO_2 / 1 bar ratio relative to the fayalite–magnetite–quartz buffer (i.e., ΔFMQ) is lower than $+2.25$) in both conditions, whereas the epidote-group mineral–garnet–quartz-bearing assemblages are stable under more oxidized conditions above the hematite–magnetite buffer (ΔFMQ $= +6.96$–15.76 and $+8.26$–14.60 in Fig. 10a and b, respectively). The latter assemblages are less oxidized than braunite-bearing assemblages (ΔFMQ > 16.44; Fig. 10) (cf., Tumiati et al., 2015). The pure piemontite–spessartine redox buffer in Tumiati et al. (2015) is absent in this study because the addition of the Fe component enlarges the stability of the epidote-group solid solution towards lower fO_2 so that an epidote-group mineral could coexist with a garnet solid solution in our Mn–Ca–Fe–Al–Si–O system (Fig. 10).

7 Bulk-rock geochemistry

Bulk-rock geochemical data of manganiferous quartzite sample 23-1F are summarized in Table S2, along with those of average values of other Mn-rich quartzose metasedimentary rocks available from the literature: the Otago schists in New Zealand (Coombs et al., 1985); Andros quartzites in Greece (Reinecke et al., 1985); Sanbagawa schists in Japan (Izadyar et al., 2003); Praborna ores of the Western Alps (Tumiati et al., 2010); Belgian coticules from the type locality, the Ardennes (Herbosch et al., 2016); and garnet-rich meta-exhalites in Venezuela (Maresch et al., 2022). The majority of the Mn-rich rocks including a quartzite sample are plotted between the Pacific–Atlantic cherts (Murray et al., 1992) and pelagic clays (Li, 2000) in the SiO_2–Al_2O_3–$Fe_2O_3^T$ diagram (Fig. 11a), except for the Belgian coticules and Venezuelan meta-exhalites. These Mn-rich quartzose rocks contain
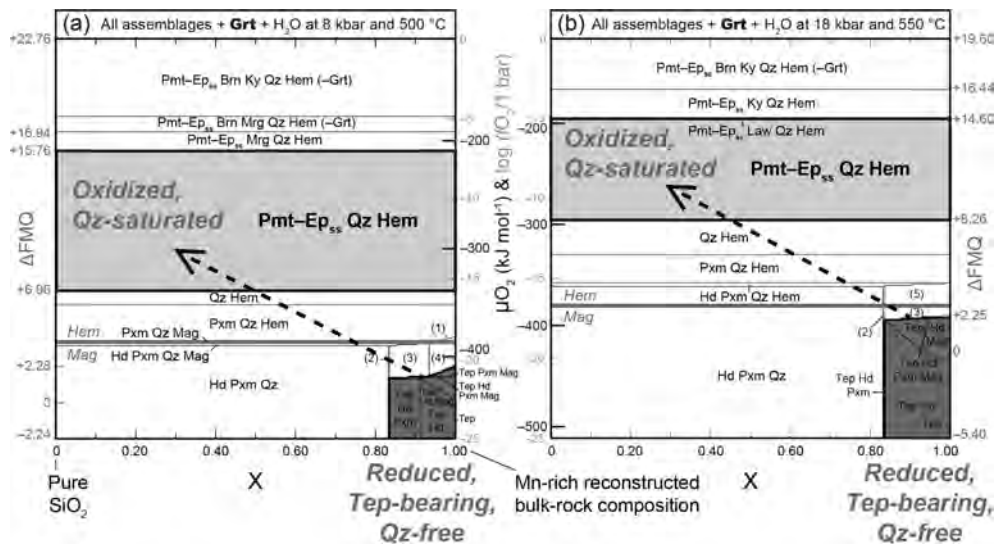
Figure 10. The μO_2 ($f O_2$ and ΔFMQ)–X diagrams of the Mn–Ca–Fe–Al–Si–O model system. $X = 0$ for pure SiO_2, and $X = 1$ for model bulk-rock composition consisting of 1 mol of garnet ($Sps_{81}Grs_{19}$), 1 mol of epidote-group mineral ($Pmt_{50}Ep_{50}$) and 0.2 mol of tephroite (Tep_{100}). Gray and dark gray fields are where the piemontite–epidote solid solution (ss) (i.e., epidote-group mineral)–hematite–quartz-bearing and tephroite-bearing assemblages are stable, respectively. Quartz-free assemblages omitted for clarity are (1) Pxm–Hem, (2) Hd–Pxm, (3) Hd–Pxm–Mag, (4) Pxm–Mag and (5) Hd–Pxm–Hem. Thick gray lines denote the hematite–magnetite buffer. Mineral abbreviations are after Whitney and Evans (2010), except for Brn for braunite.

MnO contents distinctly higher than those of the chert and pelagic clay in the Al_2O_3–MnO–$Fe_2O_3^T$ diagram (Fig. 11a), except for the talc-free piemontite–quartz schists of San-bagawa. The extent of Mn contents in the quartzite sample is comparable with and slightly higher than those of the Otago schists, piemontite $\pm$ spessartine quartzites on the island of Andros, talc-bearing piemontite–quartz schists of Sanbagawa and garnet-rich rocks in Venezuela but lower than the piemontite-free spessartine quartzites on the island of Andros, Praborna Mn ores, Belgian coticules and Fe–Mn nodules/crusts. Transition metal contents of the Mn-rich quartzose rocks are distinctly low, belonging to the hydrothermal field in the $(Cu + Ni + Co)$–Fe^T–Mn diagram, compared to that of the Fe–Mn nodules/crusts that plot in the hydrogenous field (Fig. 11b; Bonatti et al., 1972).

The rare earth element (REE) patterns of quartzite sample 23-1F normalized to those of the North American shale composite (Gromet et al., 1984) (Table S2) are characterized by a large positive Ce anomaly ($Ce/Ce^* = 2.96$) (Fig. 11c), stronger than those of the Praborna Mn ores ($Ce/Ce^* = 1.13$; Tumiati et al., 2010), Belgian coticules ($Ce/Ce^* = 1.03$; Herbosch et al., 2016), Venezuelan meta-exhalites ($Ce/Ce^* = 1.03$; Maresch et al., 2022) and Fe–Mn nodules/crusts ($Ce/Ce^* = 1.63$ and 2.59, respectively; Li, 2000) (Fig. 11c; Table S2). This geochemical feature is in marked contrast to the negative Ce anomaly ($Ce/Ce^* = 0.30$–0.55; Murray et al., 1992) shown in the Pacific–Atlantic cherts. The positive Eu anomalies represented by the Mn-rich metasediments and other oceanic

sediments ($Eu/Eu^* = 1.01$–1.55) are not prominent in the quartzite sample ($Eu/Eu^* = 0.97$). The gently positive slope of heavy REE ($Lu_N/Gd_N = 1.44$) in the sample is similar to those of the Fe–Mn crusts ($Lu_N/Gd_N = 1.21$; Li, 2000) and Venezuelan meta-exhalites ($Lu_N/Gd_N = 1.19$; Maresch et al., 2022), whereas those of others exhibit negative slopes ($Lu_N/Gd_N = 0.68$–0.83).

8   SHRIMP U–Pb ages of zircon

Zircon separates from manganiferous quartzite sample 23-1F are fine-grained ($< 100\,\mu m$), and subhedral to anhedral with aspect ratios ranging from 1 to 3 (Fig. 12a). The majority are low in CL intensity, and exhibit variable textures from patchy to oscillatory zoned patterns. The U–Th–Pb isotopic compositions of 29 spots measured on 27 zircon crystals are shown in the Tera–Wasserburg concordia diagram (Fig. 12b, c; Table S3). Nine spot dates of zircon with $> 15\,\%$ discordance were rejected from further consideration. The remaining spot analyses yielded apparent ages of the Precambrian (ca. 2155, 1894, 571, 563 and 546 Ma) with higher Th/U ratios (0.01–0.47, med. 0.07), and Cambrian (ca. 516–485 Ma) with lower Th/U ratio (0.01–0.04, med. 0.02, except for 1.73 of spot 19.1). Spot dates of the latter group yielded the weighted $^{206}Pb/^{238}U$ age of 506 ± 4 Ma ($n = 15$; MSWD (mean square weighted deviation) $= 1.13$).
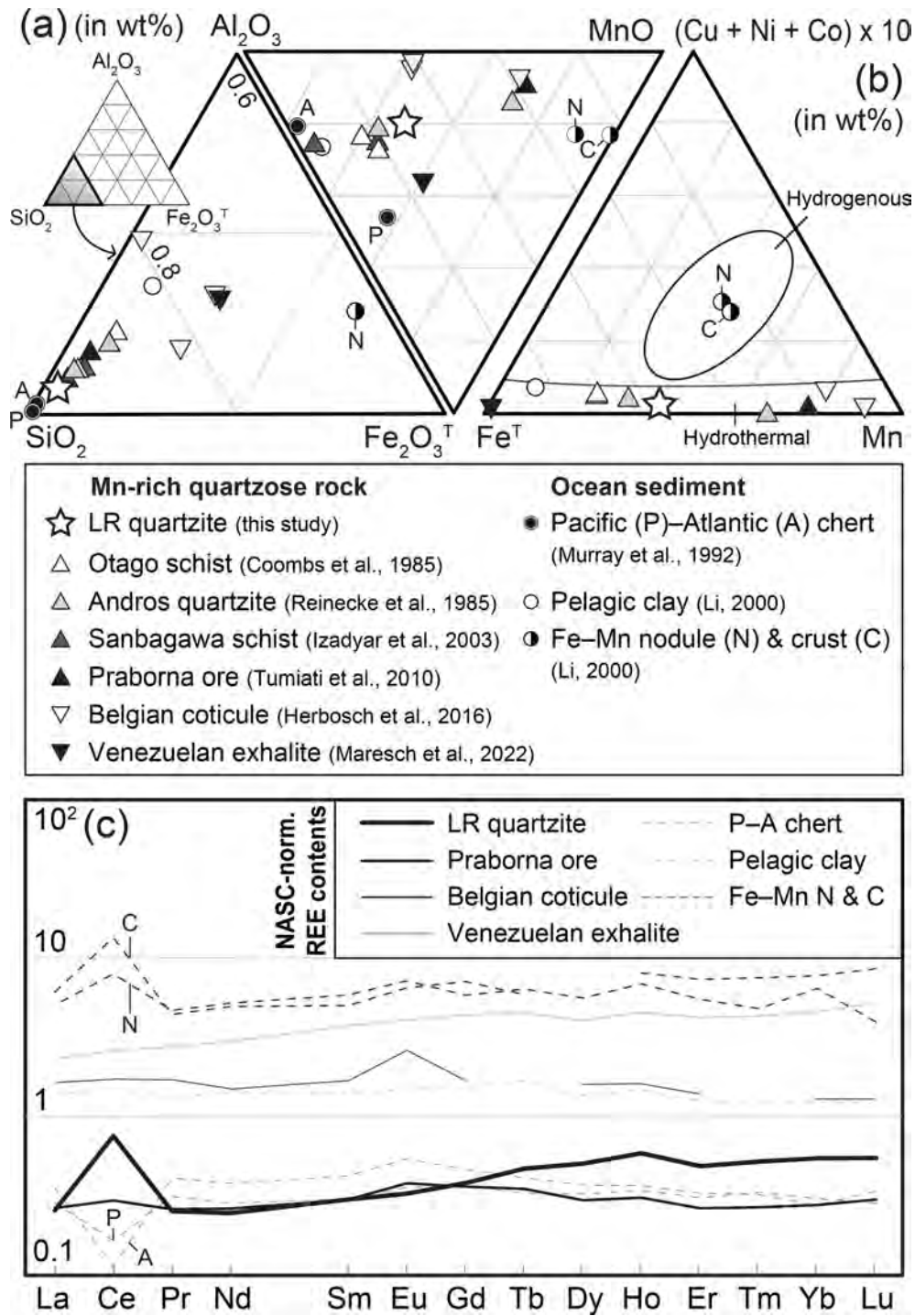
Figure 11. (a) The SiO_2–Al_2O_3–$Fe_2O_3^T$ and Al_2O_3–MnO–$Fe_2O_3^T$ and **(b)** $(Cu + Ni + Co)$–Fe–Mn ternary diagrams of the manganiferous quartzose metasediments from the Lanterman Range (LR; this study), Otago schist of New Zealand (Coombs et al., 1985), Andros of Greece (Reinecke et al., 1985), Sanbagawa belt of Japan (Izadyar et al., 2003), Praborna ore deposit of the Western Alps (Tumiati et al., 2010), Belgian coticule of the Ardennes (Herbosch et al., 2016) and garnet-rich meta-exhalite of Venezuela (Maresch et al., 2022), together with the Pacific and Atlantic Ocean cherts (Murray et al., 1992), pelagic clays, and Fe–Mn nodules/crusts (Li, 2000). The average composition of the Fe–Mn crusts is omitted in the SiO_2–Al_2O_3–$Fe_2O_3^T$ diagram because it plots outside the diagram. **(c)** Rare earth element patterns of the Mn-rich quartzose metasediments and oceanic rocks available from the literature in **(a)**, normalized (norm.) to the North American shale composite (NASC; Gromet et al., 1984).
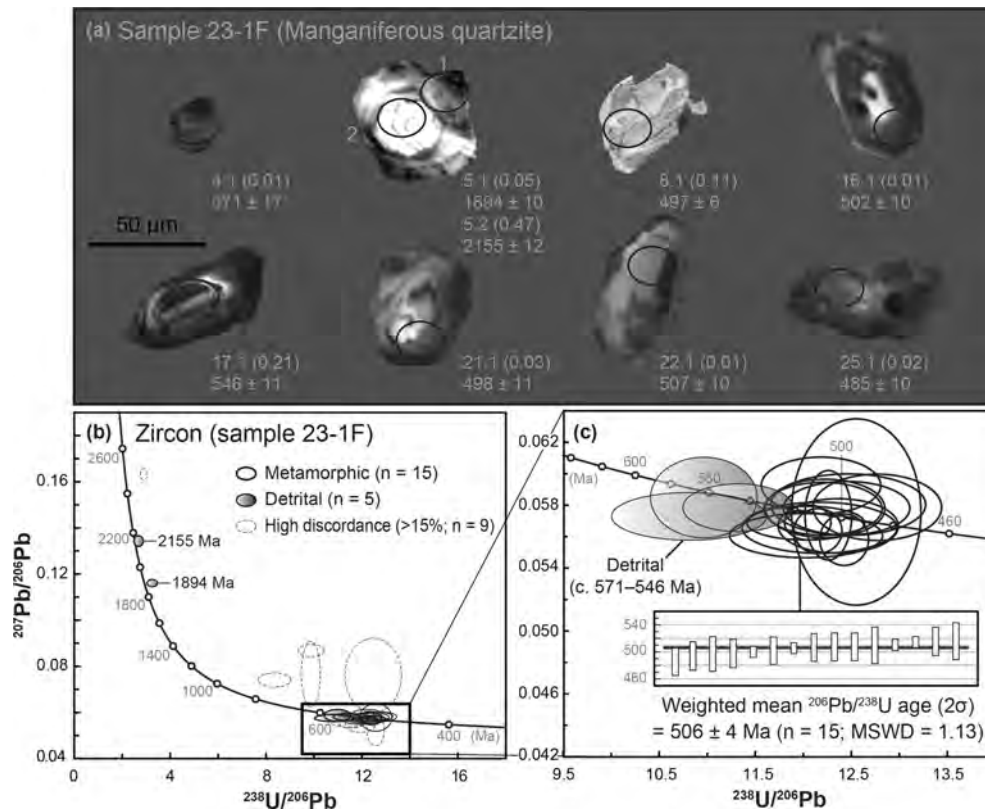
Figure 12. (a) Representative cathodoluminescence images of zircon from manganiferous quartzite sample 23-1F. Spot numbers for the U–Pb isotopic analyses listed in Table S3 are shown for individual zircon grains, followed by their Th/U ratios in parentheses. The bottom lines list the ^{206}Pb/^{238}U or ^{207}Pb/^{206}Pb dates (in Ma). Ellipses denote the SHRIMP analytical spots. **(b, c)** Tera–Wasserburg concordia diagrams showing U–Pb isotopic compositions of zircon. Error ellipses are 2σ. Dashed ellipses denote spot analyses that are excluded from the mean age calculation. Inset diagram in **(c)** shows the error bars (in 2σ) of each ^{206}Pb/^{238}U date for the weighted mean age calculation; MSWD, mean square weighted deviation.

9   Discussion

9.1   Sedimentary formation, depositional setting and formation age of the Mn-rich protolith

Deep-sea cherts or pelagic siliceous mudstones are known as protoliths of Mn-rich quartzose metasedimentary rocks, with a variety of inputs from biogenic, hydrogenous, hydrothermal and terrigenous sources (Coombs et al., 1985; Reinecke et al., 1985; Mottana, 1986; Izadyar et al., 2003; Tumiati et al., 2010). The major-element concentrations of the manganiferous quartzite sample in this study lead to chert as its probable protolith, together with minor input from pelagic clay (Fig. 11a), like other Mn-rich quartzose metasedimentary rocks except for the Belgian coticules (Herbosch et al., 2016) and Venezuelan garnet-rich rocks (Maresch et al., 2022) of limy mud turbidite and exhalite origin, respectively.

The high MnO content (1.78 wt %) and pronounced positive Ce anomaly (Ce/Ce* = 2.96) of the manganiferous quartzite sample (Fig. 11a, c) are possibly accounted for by the incorporation of the Fe–Mn nodules/crusts which are

common on the seafloor (e.g., Elderfield et al., 1981; Usui and Someya, 1997). On the basis of geochemical constraints, Reinecke et al. (1985) concluded that the Mn-nodule-bearing sediments were the primary source for the piemontite ± spessartine quartzites from the island of Andros, Greece; the nodules are now metamorphosed braunite-rich ore lenses hosted by the piemontite ± spessartine quartzites. It is noteworthy that the field occurrence of the manganiferous quartzites in the Lanterman Range as centimeter- to decimeter-thick layers is comparable with those of the piemontite ± spessartine quartzites from Andros (Reinecke et al., 1985) and piemontite quartzites in the Zermatt–Saas zone, the Western Alps (Chopin, 1978; Reinecke, 1998). Similar Mn (micro)nodules would have been present in the quartzite protolith and might have been obliterated by Cambrian high-P metamorphism during the Ross orogeny.

In the $(\mathrm{Cu + Ni + Co})$–Fe^T–Mn diagram (Fig. 11b), the manganiferous quartzite belongs to the hydrothermal deposit field where the concentration of transition metal by hydrogenous processes could be relatively weak (Bonatti, 1975; Usui and Someya, 1997). These contrasting affinities of the hy-

drogenous and hydrothermal sources could be accounted for by the dependence of element enrichment on the combination of the accumulation rate, redox condition of seawater, proximity of hydrothermal source and dilution effects from other components (e.g., Hein et al., 1997; Bau and Koschinsky, 2009). Tumiati et al. (2010) suggested a ratio of hydrogenous to hydrothermal input of 1 : 4 in the Praborna ore rocks, primarily on the basis of the degree of positive Ce anomaly (Ce/Ce* = 1.13) in the REE pattern. Thus, the proportion of the hydrogenous component in the manganiferous quartzite of this study could be higher than 1 : 4 of the Praborna case because of the far stronger positive Ce anomaly (Ce/Ce* = 2.96; Fig. 11c).

The volumetrically overwhelming garnet–phengite schists and gneisses which enclose the manganiferous quartzites in the Lanterman Range originated from continentally derived sediments in an arc/back-arc setting (Palmeri et al., 2003; Rocchi et al., 2011). Because the manganiferous quartzite is a minor lithologic unit and would share a common provenance with the host siliciclastic metasedimentary rocks, it is likely that the deep-sea chert protolith formed at a continental margin. This interpretation is supported by terrigenous input exemplified by the Paleoproterozoic (ca. 2150–1890 Ma) and late Ediacaran (ca. 570–550 Ma) detrital zircons (Fig. 12). In order to reconcile a deep-sea origin with a continental margin setting of the protolith deposition, we propose incipient extension in an arc/back-arc setting. This is partly in line with depositional settings of other Mn-rich quartzose sediments, such as a small ocean basin near a continental margin for manganiferous quartzite in Lago di Cignana, the Western Alps (Rubatto et al., 1998); a continental shelf to slope shallower than the abyssal-plain environment for the Belgian coticules (Herbosch et al., 2016); and a passive margin associated with mature back-arc extension for the Venezuelan meta-exhalites (Maresch et al., 2022), though the depositional setting differs from the oceanic spreading center environment interpreted for the Praborna Mn ore in the Saint-Marcel valley meta-ophiolite, the Western Alps (Tumiati, 2005).

The depositional timing of the chert-dominated protolith, as well the surrounding garnet–phengite quartzofeldspathic schists/gneisses, is bracketed between the youngest detrital age (ca. 546 Ma) and the metamorphic zircon age (ca. 506 Ma) (Fig. 12). This time interval does not correspond to a glacial period during Neoproterozoic (Meert and Van Der Voo, 1994), ruling out the presence of far-traveled glaciogenic detritus transported by icebergs (e.g., Porębski et al., 2019). Our results are consistent with the detrital zircon age data of Gibson et al. (2011), who proposed an upper limit of the protolith deposition of amphibolite-facies paragneisses in the Lanterman Range to be early to middle Cambrian (ca. 520–500 Ma). In addition, it is noteworthy that the latest Ediacaran maximum depositional age of the manganiferous quartzite protolith overlaps with an early phase of arc-related magmatism in NVL (e.g., Bomparola et al., 2007; Rocchi et

al., 2011). This suggests possible arc-derived local sources such as the Wilson terrane and inland cratonic Antarctica (Estrada et al., 2016; Paulsen et al., 2016; Kim et al., 2017).

9.2 High-P metamorphism, oxidation state and tectonic implications

The Mn-rich mineral assemblages of manganiferous quartzite sample 23-1F are, unfortunately, not very informative for P–T estimation (e.g., Reinecke, 1998; Izadyar et al., 2000; Tumiati et al., 2020). Therefore, we infer metamorphic stages on the basis of the mineral assemblage and compositional zonation. The Mn-rich cores of the porphyroblastic epidote-group mineral (Pmt = 0.19–0.59; Figs. 6, 7b) denote prograde metamorphism (M_1) in high-fO_2 conditions (e.g., Chopin, 1978; Bonazzi and Menchetti, 2004). This is supported by the extremely low X_{Fe} (0.00–0.07) of the spessartine-rich garnet core (Figs. 5, 7a). A rare occurrence of tephroite and rutile inclusions in the piemontite core and spessartine-rich garnet core, respectively, is consistent with blueschist-facies or low-T eclogite-facies conditions for M_1, largely depending on the oxidation state and bulk-rock composition (Fig. 10); these are based upon experimentally derived phase relationships (Abs-Wurmbach and Peters, 1999) and petrologic work on natural occurrences (e.g., Mottana, 1986; Reinecke, 1986; Tumiati, 2005).

Two sequential growth zones of epidote-group minerals (the outer domains consisting of REY-rich piemontite outer zone 1 and REY-rich epidote outer zone 2) represent prograde M_2 and peak M_3, respectively (Figs. 6, 7b, 8). The allanite enrichment trend from outer zone 1 to 2 is comparable with that reported in the eclogite-facies Mn-rich metacherts from the Praborna ore deposit, the Western Alps (Tumiati et al., 2020). These outer domains were likely produced during the prograde metamorphism at the expense of REY–Th-rich minerals such as monazite, which commonly occurs in the matrix. The paragenetic relationships between Mn–REY-rich epidote-group mineral and monazite are reminiscent of those in the eclogite-facies mica schists (Gabudianu Radulescu et al., 2009) and Barrovian metapelitic schists (Kim et al., 2009) where allanite is stable in higher-P conditions than monazite. The metamorphic peak M_3 is also represented by the celadonite-rich inner segment of phengite (Si = 3.23–3.34 apfu). The abrupt increase in X_{Fe} of garnet between the core (0.00–0.07) and rim (0.49–0.50) (Figs. 5, 7a) is tentatively attributed to a decrease in the epidote / piemontite ratio of the epidote-group mineral during $M_{2–3}$ metamorphism and an accompanying decrease in the spessartine / almandine ratio of garnet. The relatively large grain size ($\sim 500\,\mu m$ on average), largely rectilinear grain boundaries and shape preferred orientation of quartz (Fig. 4) suggest high-T grain boundary migration recrystallization (dislocation creep regime 3 of Hirth and Tullis, 1992) possibly at peak M_3. It is corroborated by the single cluster of c axes in the center and peripheral maxima of a axes typical

of dominant prism $\langle a \rangle$ slip of quartz at ~ 500–$650\,°C$ (e.g., Stipp et al., 2002).

The REY-poor epidote of the outermost domain or rim in the porphyroblastic epidote-group mineral marks retrograde stage M_4 (Tumiati et al., 2020). The exsolution of pyrophanite in titanohematite is indicative of retrograde cooling (Nakyak and Mohapatra, 1998). The chlorite growth at the expense of garnet is also a retrograde feature, which is coeval with the relatively low-celadonite outer segment of phengite (Si $= 3.14$–3.27 apfu). It is noteworthy that a marginal decomposition texture of phengite into symplectites (Palmeri et al., 2003; Kim and Lee, 2023) is absent in the manganiferous quartzite sample (Fig. 4). This suggests that the quartzite escaped significant retrogression during rapid decompression demonstrated in the surrounding garnet–phengite gneisses (Di Vincenzo and Palmeri, 2001). The aligned bands of K-feldspar and albite of near-end-member compositions parallel to the major foliation (Fig. 4a, b, c) were likely produced after the porphyroblastic epidote-group mineral or phengite during the latest stage of retrogression under $\sim 300\,°C$ (e.g., Kroll et al., 1993). The presence of two feldspars is similar to that with the low-P greenschist-facies assemblages in the late-stage fracture of the Praborna ore deposits (Tumiati et al., 2010).

The pseudosection calculation allowed us to delineate the evolution of and linkage among mineral assemblage, bulk-rock composition and oxidation state of the manganiferous quartzite (Fig. 10). The epidote-group mineral–garnet–quartz–hematite assemblage is stable under highly oxidized conditions above the hematite–magnetite buffer. The ΔFMQ values ($+6.96$ to $+15.76$ and $+8.26$ to $+14.60$) of the oxidized conditions exceed those typically observed in normal subduction settings (see Tumiati et al., 2015, and references therein) but are lower than those represented by the braunite-bearing assemblages (Tumiati, 2005; Tumiati et al., 2015). The Mn-rich, quartz-free assemblages including tephroite, which occurs as inclusions inside the epidote-group mineral (Fig. 6), are stable under relatively reduced conditions (ΔFMQ < 2.25; Fig. 10), comparable with those of the hausmannite–rhodochrosite-bearing assemblages involving the quartz-free domain of the upper levels at Praborna (Tumiati et al., 2015). Taken together, the reactive bulk-rock composition changed from Mn-rich (quartz-undersaturated, tephroite-stable) to silica-rich (quartz-present, epidote-group mineral-stable). This scenario is in harmony with the Fe–Mn nodules which would have been embedded in the chert-dominated protolith and likely homogenized with the quartzite matrix (Reinecke et al., 1985).

The metamorphic zircon age of ca. 506 Ma overlaps with those of the eclogite-facies peak stages recorded in the high-P rocks of the Lanterman Range, such as ca. 500 Ma of the boudin-shaped mafic eclogites (Di Vincenzo et al., 1997; Kim et al., 2019) and megacrystic phengite-bearing quartz vein (Kim and Lee, 2023) but is apparently younger than the ca. 530–515 Ma of prograde stages of the colder eclog-

ites and garnet–phengite quartzofeldspathic schists/gneisses (Di Vincenzo et al., 2016) (Fig. 3). The timing of the peak metamorphism is noteworthy because the juxtaposition of the Wilson and Bowers terranes also took place in the middle Cambrian in the context of the Ross orogeny (Fig. 1) (e.g., Di Vincenzo et al., 1997; Rocchi et al., 2011). Finally, we note the common depositional setting, i.e., arc/back arc, of the metachert layers and enclosing continent-derived quartzofeldspathic schists/gneisses (e.g., Palmeri et al., 2003). The deficiency of arc-derived detrital zircons in the manganiferous quartzite (Fig. 12) suggests that the deposition of the chert-like protoliths took place distally from the leading edge of the downgoing lithosphere. This paleo-position of the peculiar high-P metasedimentary rock is more amenable to exhumation in comparison to the leading edge, as suggested by numerical modeling (Warren et al., 2008), because crustal materials of the leading edge are commonly thin and cold and thus easily resist detachment. It is also consistent with the predominance of the siliciclastic metasedimentary rocks which facilitates buoyancy-driven detachment and exhumation (e.g., Ernst, 2001).

10 Conclusions

Our petrological, geochemical and geochronological results, combined with a compilation of available data on Mn-rich quartzose rocks from the literature, allowed us to characterize the sedimentary protolith and high-P metamorphism of the manganiferous quartzite layer in the Ross orogen, Antarctica. High-P metamorphism is represented by the Mn^{3+}–REY-rich epidote-group mineral–Mn^{2+}-rich garnet–phengite-bearing assemblages; porphyroblasts of the former mineral exhibit multiple growth zones, attesting to prograde to peak evolution in a highly oxidized environment. The protolith is most likely chert mixed with pelagic clay and Fe–Mn nodules, which is silica-rich and highly oxidized with a strong positive Ce anomaly. The reactive bulk-rock composition changed from Mn-rich and silica-poor to quartz-rich composition. This results in a transition from a reduced tephroite-bearing mineral assemblage to an oxidized epidote-group mineral-bearing assemblage. Zircon U–Pb ages dated the maximum age of deposition and timing of the peak eclogite-facies metamorphism (M_3) to be the latest Neoproterozoic (ca. 546 Ma) and middle Cambrian (ca. 506 Ma), respectively. The deep-sea sedimentary protolith shares a common depositional setting with the surrounding schists/gneisses of siliciclastic composition, most likely in an arc/back-arc setting of a continental margin. A lack of the Ross-arc detrital zircons further suggests that the deposition of the chert-like protolith took place distally from the leading edge of the subducting plate. This paleo-position of the protolith is amenable to exhumation of the manganiferous quartzite.

References

Abs-Wurmbach, I. and Peters, T.: The Mn-Al-Si-O system: an experimental study of phase relations applied to parageneses in manganese-rich ores and rocks, Eur. J. Mineral., 11, 45–68, https://doi.org/10.1127/ejm/11/1/0045, 1999.

Anastasiou, P. and Langer, K.: Synthesis and physical properties of piemontite $Ca_2Al_{3-p}Mn_p^{3+}$ (Si_2O_7/SiO_4/O/OH), Contrib. Mineral. Petr., 60, 225–245, https://doi.org/10.1007/BF01166798, 1977.

Armbruster, T., Bonazzi, P., Akasaka, M., Bermanec, V., Chopin, C., Gieré, R., Heuss-Assbichler, S., Liebscher, A., Menchetti, S., Pan, Y., and Pasero, M.: Recommended nomenclature of epidote-group minerals, Eur. J. Mineral., 18, 551–567, https://doi.org/10.1127/0935-1221/2006/0018-0551, 2006.

Bau, M. and Koschinsky, A.: Oxidative scavenging of cerium on hydrous Fe oxide: Evidence from the distribution of rare earth elements and yttrium between Fe oxides and Mn oxides in hydrogenetic ferromanganese crusts, Geochem. J., 43, 37–47, https://doi.org/10.2343/geochemj.1.0005, 2009.

Boger, S. D. and Miller, J. M.: Terminal suturing of Gondwana and the onset of the Ross–Delamerian Orogeny: the cause and effect of an Early Cambrian reconfiguration of plate motions, Earth Planet. Sc. Lett., 219, 35–48, 10.1016/s0012-821x(03)00692-7, 2004.

Bomparola, R. M., Ghezzo, C., Belousova, E., Griffin, W. L., and O'Reilly, S. Y.: Resetting of the U-Pb zircon system in Cambro-Ordovician intrusives of the Deep Freeze Range, Northern Victoria Land, Antarctica, J. Petrol., 48, 327–364, https://doi.org/10.1093/petrology/egl064, 2007.

Bonatti, E.: Metallogenesis at Oceanic Spreading Centers, Annu. Rev. Earth Planet. Sc., 3, 401–431, https://doi.org/10.1146/annurev.ea.03.050175.002153, 1975.

Bonatti, E., Fisher, D. E., Joensuu, O., Rydell, H. S., and Beyth, M.: Iron-manganese-barium deposit from the Northern Afar Rift (Ethiopia), Econ. Geol., 67, 717–730, https://doi.org/10.2113/gsecongeo.67.6.717, 1972.

Bonazzi, P. and Menchetti, S.: Manganese in Monoclinic Members of the Epidote Group: Piemontite and Related Minerals, Rev. Mineral. Geochem., 56, 495–552, https://doi.org/10.2138/gsrmg.56.1.495, 2004.

Borg, S. G., Stump, E., Chappell, B. W., Mcculloch, M. T., Wyborn, D., Armstrong, R. L., and Holloway, J. R.: Granitoids of northern Victoria Land, Antarctica – Implications of chemical and isotopic variations to regional crustal structure and tectonics, Am. J. Sci., 287, 127–169, https://doi.org/10.2475/ajs.287.2.127, 1987.

Bradshaw, J. D., Weaver, S., and Laird, M. G.: Suspect terranes and Cambrian tectonics in northern Victoria Land, Antarctica, in: Tectonostratigraphic Terranes of the Circum-Pacific Region, edited by: Howell, D. G., Earth Science Series, 1, Circum-Pacific Council for Energy and Mineral Resources, Houston, 467–479, ISBN 978-0933687004, 1985.

Bunge, H. J.: 2 – Orientation of Individual Crystallites, in: Texture Analysis in Materials Science, edited by: Bunge, H. J., Butterworth-Heinemann, 3–41, https://doi.org/10.1016/B978-0-408-10642-9.50007-6, 1982.

Capponi, G., Castelli, D., Fioretti, A. M., and Oggiano, G.: Geological mapping and field relationships of eclogites from the Lanterman Range (northern Victoria Land, Antarctica), in: The Antarctic Region: Geological Evolution and Processes, edited by: Ricci,

C. A., Terra Antarctica Publication, Siena, 219–225, ISBN 978-8890022104, 1997.

Carswell, D. A.: Eclogite Facies Rocks, Springer Dordrecht, 396 pp., ISBN 978-9401092654, 1990.

Cawood, P. A.: Terra Australis Orogen: Rodinia breakup and development of the Pacific and Iapetus margins of Gondwana during the Neoproterozoic and Paleozoic, Earth-Sci. Rev., 69, 249–279, https://doi.org/10.1016/j.earscirev.2004.09.001, 2005.

Cenki-Tok, B. and Chopin, C.: Coexisting calderite and spessartine garnets in eclogite-facies metacherts of the Western Alps, Mineral. Petrol., 88, 47–68, https://doi.org/10.1007/s00710-006-0146-4, 2006.

Cheong, W., Cho, M., and Kim, Y.: An efficient method for zircon separation using the gold pan, Journal of the Petrological Society of Korea, 22, 63–70, https://doi.org/10.7854/jpsk.2013.22.1.063, 2013.

Chopin, C.: Les paragenèses réduites ou oxydées de concentrations manganésifères des "schistes lustrés" de Haute-Maurienne (Alpes françaises), B. Minéral., 101, 514–531, https://doi.org/10.3406/bulmi.1978.7222, 1978.

Claoué-Long, J. C., Compston, W., Roberts, J., and Fanning, C. M.: Two Carboniferous ages: A comparison of SHRIMP zircon dating with conventional zircon ages and $^{40}Ar/^{39}Ar$ analysis, in: Geochronology, Time Scales and Global Stratigraphic Correlation, edited by: Berggren, W. A., Kent, D. V., Aubry, M. P., and Hardenbol, J., SEPM Society for Sedimentary Geology, https://doi.org/10.2110/pec.95.04.0003, 1995.

Connolly, J. A. D.: Computation of phase equilibria by linear programming: A tool for geodynamic modeling and its application to subduction zone decarbonation, Earth Planet. Sc. Lett., 236, 524–541, https://doi.org/10.1016/j.epsl.2005.04.033, 2005.

Coombs, D. S., Dowse, M., Grapes, R., Kawachi, Y., and Roser, B.: Geochemistry and origin of piemontite-bearing and associated manganiferous schists from Arrow Junction, Western Otago, New Zealand, Chem. Geol., 48, 57–78, https://doi.org/10.1016/0009-2541(85)90035-X, 1985.

Cumming, G. L. and Richards, J. R.: Ore lead isotope ratios in a continuously changing earth, Earth Planet. Sc. Lett., 28, 155–171, https://doi.org/10.1016/0012-821X(75)90223-X, 1975.

Dallmeyer, R. D. and Wright, T. O.: Diachronous cleavage development in the Robertson Bay terrane, Northern Victoria Land, Antarctica: Tectonic implications, Tectonics, 11, 437–448, https://doi.org/10.1029/91TC02891, 1992.

Di Vincenzo, G. and Palmeri, R.: An $^{40}Ar-^{39}Ar$ investigation of high-pressure metamorphism and the retrogressive history of mafic eclogites from the Lanterman Range (Antarctica): evidence against a simple temperature control on argon transport in amphibole, Contrib. Mineral. Petr., 141, 15–35, https://doi.org/10.1007/s004100000226, 2001.

Di Vincenzo, G., Palmeri, R., Talarico, F., Andriessen, P. A. M., and Ricci, C. A.: Petrology and geochronology of eclogites from the Lanterman Range, Antarctica, J. Petrol., 38, 1391–1417, https://doi.org/10.1093/petroj/38.10.1391, 1997.

Di Vincenzo, G., Ghiribelli, B., Giorgetti, G., and Palmeri, R.: Evidence of a close link between petrology and isotope records: constraints from SEM, EMP, TEM and in situ $^{40}Ar-^{39}Ar$ analyses on multiple generations of white micas (Lanterman Range, Antarctica), Earth Planet. Sc. Lett., 192, 389–405, https://doi.org/10.1016/S0012-821X(01)00454-X, 2001.

Di Vincenzo, G., Horton, F., and Palmeri, R.: Protracted (~ 30 Ma) eclogite-facies metamorphism in northern Victoria Land (Antarctica): Implications for the geodynamics of the Ross/Delamerian Orogen, Gondwana Res., 40, 91–106, https://doi.org/10.1016/j.gr.2016.08.005, 2016.

Edmond, J. M., Von Damm, K. L., McDuff, R. E., and Measures, C. I.: Chemistry of hot springs on the East Pacific Rise and their effluent dispersal, Nature, 297, 187–191, https://doi.org/10.1038/297187a0, 1982.

Elderfield, H., Hawkesworth, C. J., Greaves, M. J., and Calvert, S. E.: Rare earth element geochemistry of oceanic ferromanganese nodules and associated sediments, Earth Planet. Sc. Lett., 45, 513–528, https://doi.org/10.1016/0016-7037(81)90184-8, 1981.

Ernst, W. G.: Subduction, ultrahigh-pressure metamorphism, and regurgitation of buoyant crustal slices – implications for arcs and continental growth, Phys. Earth Planet. In., 127, 253–275 https://doi.org/10.1016/S0031-9201(01)00231-X, 2001.

Estrada, S., Läufer, A., Eckelmann, K., Hofmann, M., Gärtner, A., and Linnemann, U.: Continuous Neoproterozoic to Ordovician sedimentation at the East Gondwana margin – Implications from detrital zircons of the Ross Orogen in northern Victoria Land, Antarctica, Gondwana Res., 37, 426–448, https://doi.org/10.1016/j.gr.2015.10.006, 2016.

Faure, G. and Mensing, T. M.: The Transantarctic Mountains – Rocks, Ices, Meteorites, and Water, Springer Dordrecht, 600 pp., https://doi.org/10.1007/978-90-481-9390-5, 2010.

Field, B. D. and Findlay, R. H.: The sedimentology of the Robertson Bay Group, northern Victoria Land, in: Antarctic Earth Science, edited by: Oliver, R. L., James, P. R., and Jago, J. B., Australian Academy of Science, Canberra, 102–106, ISBN 978-0521258364, 1983.

Foden, J., Elburg, M. A., Dougherty-Page, J., and Burtt, A.: The timing and duration of the Delamerian Orogeny: Correlation with the Ross Orogen and implications for Gondwana assembly, J. Geol., 114, 189–210, https://doi.org/10.1086/499570, 2006.

Gabudianu Radulescu, I., Rubatto, D., Gregory, C., and Compagnoni, R.: The age of HP metamorphism in the Gran Paradiso Massif, Western Alps: A petrological and geochronological study of "silvery micaschists", Lithos, 110, 95–108, https://doi.org/10.1016/j.lithos.2008.12.008, 2009.

GANOVEX Team: Geological map of North Victoria Land, Antarctica, 1 : 500000 – Explanatory Notes, in: German Antarctic North Victoria Land Expedition (GANOVEX III), edited by: Tessensohn, F. and Roland, N. W., Geologisches Jahrbuch, B66, Bundesanstalt für Geowissenschaften und Rohstoffe, Hannover, 7–79, ISBN 978-3-510-96279-2, 1987.

Ghiribelli, B., Frezzotti, M.-L., and Palmeri, R.: Coesite in eclogites of the Lanterman Range (Antarctica): Evidence from textural and Raman studies, Eur. J. Mineral., 14, 355–360, https://doi.org/10.1127/0935-1221/2002/0014-0355, 2002.

Giacomini, F., Tiepolo, M., Dallai, L., and Ghezzo, C.: On the onset and evolution of the Ross-orogeny magmatism in North Victoria Land – Antarctica, Chem. Geol., 240, 103–128, https://doi.org/10.1016/j.chemgeo.2007.02.005, 2007.

Gibson, G. M., Morse, M. P., Ireland, T. R., and Nayak, G. K.: Arc–continent collision and orogenesis in western Tasmanides: Insights from reactivated basement structures and formation of an ocean–continent transform bound-

ary off western Tasmania, Gondwana Res., 19, 608–627, https://doi.org/10.1016/j.gr.2010.11.020, 2011.

Goodge, J. W.: Geological and tectonic evolution of the Transantarctic Mountains, from ancient craton to recent enigma, Gondwana Res., 80, 50–122, https://doi.org/10.1016/j.gr.2019.11.001, 2020.

Goodge, J. W. and Dallmeyer, R. D.: Contrasting thermal evolution within the Ross orogen, Antarctica: Evidence from mineral $^{40}Ar/^{39}Ar$ ages, J. Geol., 104, 435–458, https://doi.org/10.1086/629838, 1996.

Grew, E. S., Kleinschmidt, G., and Schubert, W.: Contrasting metamorphic belts in north Victoria Land, Antarctica, in: German Antarctic North Victoria Land Expedition (GANOVEX III), edited by: Roland, N. W., Geologisches Jahrbuch, B60, Bundesanstalt für Geowissenschaften und Rohstoffe, Hannover, 253–263, ISBN 978-3-510-96285-3, 1984.

Gromet, L. P., Dymek, R. F., Haskin, L. A., and Korotev, R. L.: The "North American shale composite": Its compilation, major and trace element characteristics, Geochim. Cosmochim. Ac., 48, 2469–2482, https://doi.org/10.1016/0016-7037(84)90298-9, 1984.

Guidotti, C. V.: Micas in metamorphic rocks, Rev. Mineral. Geochem., 13, 357–467, 1984.

Hein, J. R., Koschinsky, A., Halbach, P., Manheim, F. T., Bau, M., Kang, J.-K., and Lubick, N.: Iron and manganese oxide mineralization in the Pacific, in: Manganese Mineralization: Geochemistry and Mineralogy of Terrestrial and Marine Deposit, edited by: Nicholson, K., Hein, J. R., Bühn, B., and Dasgupta, S., 119, Geological Society, London, Special Publications, 123–138, https://doi.org/10.1144/GSL.SP.1997.119.01.09, 1997.

Herbosch, A., Liégeois, J.-P., and Pin, C.: Coticules of the Belgian type area (Stavelot-Venn Massif): Limy turbidites within the nascent Rheic oceanic basin, Earth-Sci. Rev., 159, 186–214, 10.1016/j.earscirev.2016.05.012, 2016.

Hirth, G. and Tullis, J.: Dislocation creep regimes in quartz aggregates, J. Struct. Geol., 14, 145–159, https://doi.org/10.1016/0191-8141(92)90053-Y, 1992.

Holland, T. J. B. and Powell, R.: An internally consistent thermodynamic data set for phases of petrological interest, J. Metamorph. Geol., 16, 309–343, https://doi.org/10.1111/j.1525-1314.1998.00140.x, 1998.

Izadyar, J., Hirajima, T., and Nakamura, D.: Talc-phengite-albite assemblage in piemontite-quartz schist of the Sanbagawa metamorphic belt, central Shikoku, Japan, Isl. Arc., 9, 145–158, https://doi.org/10.1046/j.1440-1738.2000.00268.x, 2000.

Izadyar, J., Tomita, K., and Shinjoe, H.: Geochemistry and origin of piemontite-quartz schists in the Sanbagawa Metamorphic Belt, central Shikoku, Japan, J. Asian Earth Sci., 21, 711–730, https://doi.org/10.1016/S1367-9120(02)00029-9, 2003.

Jago, J. B., Bentley, C. J., and Cooper, R. A.: Cambrian biostratigraphy of the Bowers back-arc basin, Northern Victoria Land, Antarctica – A review, Palaeoworld, 28, 276–288, https://doi.org/10.1016/j.palwor.2018.12.002, 2019.

Keskinen, M. and Liou, J. G.: Synthesis and stability relations of Mn-Al piemontite, $Ca_2MnAl_2Si_3O_{12}(OH)$, Am. Mineral., 64, 317–328, 1979.

Kim, T. and Lee, M. J.: U-Pb ages and REE compositions of zircon in megacrystic phengite-bearing quartz vein from the Lanterman

Range, northern Victoria Land, Antarctica, Geochem. J., 57, 1–12, https://doi.org/10.2343/geochemj.GJ23001, 2023.

Kim, T., Kim, Y., Cho, M., and Lee, J. I.: P–T evolution and episodic zircon growth in barroisite eclogites of the Lanterman Range, northern Victoria Land, Antarctica, J. Metamorph. Geol., 37, 509–537, https://doi.org/10.1111/jmg.12474, 2019.

Kim, T., Kim, Y., Cheong, W., Cho, M., and Lee, J. I.: Ediacaran mafic magmatism recorded in Cambrian eclogites of the Ross orogen, Antarctica: Implications for the Neoproterozoic rifting episodes along the Pacific-Gondwana margin, Terra Nova, 35, 32–40, https://doi.org/10.1111/ter.12626, 2023.

Kim, Y., Yi, K., and Cho, M.: Parageneses and Th-U distributions among allanite, monazite, and xenotime in Barrovian-type metapelites, Imjingang belt, central Korea, Am. Mineral., 94, 430–438, https://doi.org/10.2138/am.2009.2769, 2009.

Kim, Y., Kim, T., Lee, J. I., and Kim, S. J.: SHRIMP U-Pb ages of zircon from banded gneisses and a leucocratic dyke in the Wilson Terrane, northern Victoria Land, Antarctica, Journal of the Geological Society of Korea, 53, 489–507, https://doi.org/10.14770/jgsk.2017.53.4.489, 2017.

Kleinschmidt, G. and Tessensohn, F.: Early Paleozoic Westward Directed Subduction at the Pacific Margin of Antarica, in: Gondwana Six: Structure, Tectonics, and Geophysics, edited by: McKenzie, G. D., American Geophysical Union, Washington, D.C., 89–105, https://doi.org/10.1029/GM040p0089, 1987.

Kroll, H., Evangelakakis, C., and Voll, G.: Two-feldspar geothermometry: a review and revision for slowly cooled rocks, Contrib. Mineral. Petr., 114, 510–518, https://doi.org/10.1007/BF00321755, 1993.

Läufer, A. L., Lisker, F., and Phillips, G.: Late ross-orogenic deformation of basement rocks in the northern deep freeze range, Victoria Land, Antarctica: the Lichen Hills shear zone, Polarforschung, 80, 60–70, 2011.

Li, Y. H.: A Compendium of Geochemistry: From Solar Nebula to the Human Brain, Princeton University Press, Princeton, 440 pp., https://doi.org/10.1515/9780691229515, 2000.

Ludwig, K. R.: User's manual for Isoplot 3.6: A geochronological toolkit for Microsoft Excel, Special Publication, Berkeley Geochronology Center, 77 pp., 2008.

Ludwig, K. R.: SQUID 2: A User's Manual, Berkeley Geochronology Center Special Publication, 100 pp., 2009.

Maresch, W. V., Stanek, K. P., Speich, L., Schertl, H.-P., and Villagómez, D.: Garnetite, garnet-quartz ("coticule") and calc-silicate layers in high-pressure metapelitic rocks, Venezuela: metamorphosed exhalites in a Cretaceous back-arc basin, Int. Geol. Rev., 64, 885–910, https://doi.org/10.1080/00206814.2021.1891978, 2022.

Massonne, H. J. and Schreyer, W.: Stability field of the high-pressure assemblage talc + phengite and two new phengite barometers, Eur. J. Mineral., 1, 391–410, 1989.

Meert, J. G. and van der Voo, R.: The Neoproterozoic (1000–540 Ma) glacial intervals: No more snowball earth?, Earth Planet. Sc. Lett., 123, 1–13, 1994.

Melcher, F.: Genesis of chemical sediments in Birimian greenstone belts: evidence from gondites and related manganese-bearing rocks from northern Ghana, Mineral. Mag., 59, 229–251, https://doi.org/10.1180/minmag.1995.059.395.08, 1995.

Mottana, A.: Blueschist-facies metamorphism of manganiferous cherts: A review of the alpine occurrences, in: Blueschists and

Eclogites, edited by: Evans, B. W. and Brown, E. H., Geological Society of America Memoir, 164, Geological Society of America, 267–299, https://doi.org/10.1130/MEM164, 1986.

Murray, R. W., Buchholtz ten Brink, M. R., Gerlach, D. C., Russ, G. P., and Jones, D. L.: Interoceanic variation in the rare earth, major, and trace element depositional chemistry of chert: Perspectives gained from the DSDP and ODP record, Geochim. Cosmochim. Ac., 56, 1897–1913, https://doi.org/10.1016/0016-7037(92)90319-E, 1992.

Nakyak, B. R. and Mohapatra, B. K.: Two morphologies of pyrophanite in Mn-rich assemblages, Gangpur Group, India, Mineral. Mag., 62, 847–856, https://doi.org/10.1180/002646198548070, 1998.

Paces, J. B. and Miller, J. D.: Precise U-Pb ages of Duluth Complex and related mafic intrusions, northeastern Minnesota: Geochronological insights to physical, petrogenetic, paleomagnetic, and tectonomagmatic processes associated with the 1.1 Ga Midcontinent Rift system, J. Geophys. Res., 98, 13997–14013, https://doi.org/10.1029/93jb01159, 1993.

Page, F. Z., Armstrong, L. S., Essene, E. J., and Mukasa, S. B.: Prograde and retrograde history of the Junction School eclogite, California, and an evaluation of garnet–phengite–clinopyroxene thermobarometry, Contrib. Mineral. Petr., 153, 533–555, https://doi.org/10.1007/s00410-006-0161-9, 2007.

Palmeri, R.: $P–T$ paths and migmatite formation: An example from Deep Freeze Range, northern Victoria Land, Antarctica, Lithos, 42, 47–66, https://doi.org/10.1016/S0024-4937(97)00036-4, 1997.

Palmeri, R., Ghiribelli, B., Talarico, F., and Ricci, C. A.: Ultrahigh-pressure metamorphism in felsic rocks: the garnet-phengite gneisses and quarzites from the Lanterman Range, Antarctica, Eur. J. Mineral., 15, 513–525, https://doi.org/10.1127/0935-1221/2003/0015-0513, 2003.

Palmeri, R., Sandroni, S., Godard, G., and Ricci, C. A.: Boninite-derived amphibolites from the Lanterman-Mariner suture (northern Victoria Land, Antarctica): New geochemical and petrological data, Lithos, 140–141, 200–223, https://doi.org/10.1016/j.lithos.2012.02.001, 2012.

Paulsen, T. S., Deering, C., Sliwinski, J., Bachmann, O., and Guillong, M.: Detrital zircon ages from the Ross Supergroup, north Victoria Land, Antarctica: Implications for the tectonostratigraphic evolution of the Pacific-Gondwana margin, Gondwana Res., 35, 79–96, https://doi.org/10.1016/j.gr.2016.04.001, 2016.

Porêbski, S. J., Anczkiewicz, R., Paszkowski, M., Skompski, S., Kêdzior, A., Mazur, S., Szczepañski, J., Buniak, A., and Mikołajewski, Z.: Hirnantian icebergs in the subtropical shelf of Baltica: Evidence from sedimentology and detrital zircon provenance, Geology, 47, 284–288, https://doi.org/10.1130/g45777.1, 2019.

Reinecke, T.: Phase relationships of sursassite and other Mn-silicates in highly oxidized low-grade, high-pressure metamorphic rocks from Evvia and Andros Islands, Greece, Contrib. Mineral. Petr., 94, 110–126, https://doi.org/10.1007/BF00371232, 1986.

Reinecke, T.: Prograde high- to ultrahigh-pressure metamorphism and exhumation of oceanic sediments at Lago di Cignana, Zermatt-Saas Zone, western Alps, Lithos, 42, 147–189, https://doi.org/10.1016/S0024-4937(97)00041-8, 1998.

Reinecke, T., Okrusch, M., and Richter, P.: Geochemistry of ferromanganoan metasediments from the Island of Andros, Cy-

cladic Blueschist Belt, Greece, Chem. Geol., 53, 249–278, https://doi.org/10.1016/0009-2541(85)90074-9, 1985.

Ricci, C. A., Talarico, F., Palmeri, R., Di Vincenzo, G., and Pertusati, P. C.: Eclogite at the Antarctic palaeo-Pacific active margin of Gondwana (Lanterman Range, northern Victoria Land, Antarctica), Antarct. Sci., 8, 277–280, https://doi.org/10.1017/S0954102096000399, 1996.

Rocchi, S., Di Vincenzo, G., and Ghezzo, C.: The Terra Nova Intrusive Complex (Victoria Land, Antarctica), Terra Antartica Reports, Terra Antartica Publication. 49 pp., 2004.

Rocchi, S., Bracciali, L., Di Vincenzo, G., Gemelli, M., and Ghezzo, C.: Arc accretion to the early Paleozoic Antarctic margin of Gondwana in Victoria Land, Gondwana Res., 19, 594–607, https://doi.org/10.1016/j.gr.2010.08.001, 2011.

Rubatto, D., Gebauer, D., and Fanning, M.: Jurassic formation and Eocene subduction of the Zermatt–Saas-Fee ophiolites: implications for the geodynamic evolution of the Central and Western Alps, Contrib. Mineral. Petr., 132, 269–287, https://doi.org/10.1007/s004100050421, 1998.

Scambelluri, M., Messiga, B., Vannucci, R., and Villa, I. M.: Petrology, geochemistry and geochronology of the Dessent Unit, northern Victoria Land, Antarctica: Some constraints on its evolutionary history, in: Aspects of a Suture Zone – Mariner Glacier Area, Antarctica, edited by: Tessenshon, F., and Ricci, C. A., Geologisches Jahrbuch, B85, Bundesanstalt für Geowissenschaften und Rohstoffe, Hannover, 95–131, 2003.

Skemer, P., Katayama, I., Jiang, Z., and Karato, S.-I.: The misorientation index: Development of a new method for calculating the strength of lattice-preferred orientation, Tectonophysics, 411, 157–167, https://doi.org/10.1016/j.tecto.2005.08.023, 2005.

Stipp, M., Stünitz, H., Heilbronner, R., and Schmid, S. M.: The eastern Tonale fault zone: a "natural laboratory" for crystal plastic deformation of quartz over a temperature range from 250 to 700 °C, J. Struct. Geol., 24, 1861–1884, https://doi.org/10.1016/S0191-8141(02)00035-4, 2002.

Stump, E.: The Ross Orogen of the Transantarctic Mountains, Cambridge University Press, Cambridge, UK, 284 pp., ISBN 9780521019996, 1995.

Sun, S. S. and McDonough, W. F.: Chemical and isotopic systematics of oceanic basalts: implications for mantle composition and processes, in: Magmatism in the Ocean Basins, edited by: Saunders, A. D. and Norry, M. J., 42, Geological Society, London, Special Publications, 313–345, https://doi.org/10.1144/gsl.sp.1989.042.01.19, 1989.

Talarico, F., Ghiribelli, B., Siddoway, C. S., Palmeri, R., and Ricci, C. A.: The northern Victoria Land segment of the Antarctic paleo-Pacific margin of eastern Gondwana: new constraints from the Lanterman and Mountaineer ranges, Terra Antartica, 5, 245–252, 1998.

Talarico, F. M., Palmeri, R., and Ricci, C. A.: Regional metamorphism and P-T evolution of the Ross Orogen in northern Victoria Land (Antarctica): a review, Period. Mineral., 73, 185–196, 2004.

Thomson, J. A.: Relationships of coticule geochemistry to stratigraphy in the Perry Mountain and Megunticook formations, New England Appalachians, Can. Mineral., 39, 1021–1037, https://doi.org/10.2113/gscanmin.39.4.1021, 2001.

Tumiati, S.: Geochemistry, mineralogy and petrology of the eclogitized manganese deposit of Praborna (Valle d'Aosta, Western

Italian Alps), PhD thesis, Università degli Studi dell'Insubria and Université Paris, 7, 241 pp., 2005.

Tumiati, S., Martin, S., and Godard, G.: Hydrothermal origin of manganese in the high-pressure ophiolite metasediments of Praborna ore deposit (Aosta Valley, Western Alps), Eur. J. Mineral., 22, 577–594, https://doi.org/10.1127/0935-1221/2010/0022-2035, 2010.

Tumiati, S., Godard, G., Martin, S., Malaspina, N., and Poli, S.: Ultra-oxidized rocks in subduction mélanges? Decoupling between oxygen fugacity and oxygen availability in a Mn-rich metasomatic environment, Lithos, 226, 116–130, https://doi.org/10.1016/j.lithos.2014.12.008, 2015.

Tumiati, S., Merlini, M., Godard, G., Hanfland, M., and Fumagalli, P.: Orthovanadate wakefieldite-(Ce) in symplectites replacing vanadium-bearing omphacite in the ultra-oxidized manganese deposit of Praborna (Aosta Valley, Western Italian Alps), Am. Mineral., 105, 1242–1253, https://doi.org/10.2138/am-2020-7219, 2020.

Usui, A. and Someya, M.: Distribution and composition of marine hydrogenetic and hydrothermal manganese deposits in the northwest Pacific, in: Manganese Mineralization: Geochemistry and Mineralogy of Terrestrial and Marine Deposit, edited by: Nicholson, K., Hein, J. R., Bühn, B., and Dasgupta, S., 119, Geological Society, London, Special Publications, 177–198, https://doi.org/10.1144/GSL.SP.1997.119.01.12, 1997.

Warren, C. J., Beaumont, C., and Jamieson, R. A.: Modelling tectonic styles and ultra-high pressure (UHP) rock exhumation during the transition from oceanic subduction to continental collision, Earth Planet. Sc. Lett., 267, 129–145, https://doi.org/10.1016/j.epsl.2007.11.025, 2008.

Weaver, S. D., Bradshaw, J. D., and Laird, M. G.: Geochemistry of Cambrian volcanics of the Bowers Supergroup and implications for the Early Palaeozoic tectonic evolution of northern Victoria Land, Antarctica, Earth Planet. Sc. Lett., 68, 128–140, https://doi.org/10.1016/0012-821X(84)90145-6, 1984.

Whitney, D. L. and Evans, B. W.: Abbreviations for names of rock-forming minerals, Am. Mineral., 95, 185–187, https://doi.org/10.2138/am.2010.3371, 2010.

Williams, I. S.: U-Th-Pb geochronology by Ion Microprobe, in: Applications of microanalytical techniques to understanding mineralizing processes, edited by: McKibben, M. A., Shanks III, W. C., and Ridley, W. I., 1–35, https://doi.org/10.5382/Rev.07.01, 1998.

Wodzicki, A. and Robert Jr., R.: Geology of the Bowers Supergroup, central Bowers Mountains, northern Victoria Land, in: Geological Investigations in Northern Victoria Land, edited by: Stump, E., Antarctic Research Series, American Geophysical Union, Washington, D.C., 39–68, https://doi.org/10.1002/9781118664957.ch3, 1986.

Zhen, Y. Y., Percival, I. G., Woo, J., and Park, T.-Y. S.: Latest Cambrian–earliest Ordovician conodonts and microbrachiopods from northern Victoria Land, Antarctica: Handler Ridge revisited, Palaeoworld, 28, 13–23, https://doi.org/10.1016/j.palwor.2018.03.004, 2019.